

EXPERIMENTAL INVESTIGATION ON THE VISCOSITY, ELECTRICAL CONDUCTIVITY AND PH OF SiO₂-ETHYLENE GLYCOL NANOFLUIDS

Sharifpur M.*, Adio S.A. and Meyer J.P.

*Author for correspondence

Department of Mechanical and Aeronautical Engineering,
University of Pretoria,
Pretoria, 0002,
South Africa,

E-mail: mohsen.sharifpur@up.ac.za

ABSTRACT

Nanofluids are new heat transfer fluid aimed at mitigating the poor heat removal efficiency of the conventional heat transfer fluids. Previous reports showed that nanofluids prepared from conventional heat transfer fluids have higher thermal conductivity compared to the constituent base fluids such as water or ethylene glycol. However not much have been done in other areas especially on the viscosity, electrical conductivity and pH. In this paper, experimental investigations were carried out on SiO₂ nanoparticles dispersed in ethylene glycol at two different energy densities using ultrasound assist mechanism. The SiO₂ nanoparticles used have an average particle size (APS) 13.4±5.6 nm. The combined effect of temperature, volume fraction and energy density on the viscosity, electrical conductivity and pH of the nanofluids were investigated. The temperature range investigated was between 20-70°C, volume fraction between 0-5%, and energy density of 1.5×10⁵ kJ/m³ and 3.2×10⁵ kJ/m³. The results showed temperature and volume fraction have significant influence on the viscosity, electrical conductivity and pH of the nanofluids. However, the energy density shows no significance on the viscosity of the nanofluids which was dependent on the level of dispersion of the suspension.

INTRODUCTION

Waste heat recovery and cooling are processes that have been integrated into many industrial systems, such as in the oil and gas, pulp and paper, food, power generation and textile industries. These processes require that heat recovery and/or cooling is mostly performed by means of a flowing fluid. In the past decades ethylene glycol (EG), glycerol, water and oil are some of the conventional heat transfer fluids that have been used for this purpose. However, these conventional heat transfer fluids are characteristically poor with regards to their thermal properties. In order to improve the obviously poor thermal properties (especially specific heat and thermal conductivity) of the conventional heat transfer fluids, particle dispersion in heat transfer fluids (fluid bases) was proposed by Maxwell in the 19th century [1]. Due to the lack of technology to produce particles smaller than the micrometric size at the time, numerous engineering problems such as equipment clogging, abrasion, particle settlement and severe pressure drop

NOMENCLATURE

p	[-]	Coefficient of primary electroviscous effect
a	[m]	Particle radius
k_B	[W/m ² K ⁴]	Stephan Boltzmann constant
T	[°K]	Absolute temperature
N_A	[mole ⁻¹]	Avogadro's number
e	[C]	Elementary charge
I	[moles/m ³]	Ionic strength
Special characters		
ϕ	[-]	Volume fraction ratio
ϱ	[-]	Coefficient of secondary electroviscous effect
η	[-]	Intrinsic viscosity
μ	Pa.s	Viscosity
κ	[m]	Inverse of Debye length
ϵ_0	[C ² .N ⁻¹ .m ⁻²]	Permittivity of the vacuum
ϵ_r	[-]	Dielectric constant for the medium
Subscripts		
o		Fluid base
r	[-]	Relative

were encountered. Modern knowledge and technological advancements made it possible for the production of nanosized materials and recently, Choi and Eastman [2] suspended nanoparticles of Cu in water to produced Cu-H₂O nanofluid. Nanofluid has the potential to enhance the heat transfer rate in industrial equipment thus making industrial heat exchangers more compact. Consequently, this will reduce the energy consumption and emission levels (reduced greenhouse gases and global warming potential).

Unlike previous suspensions with millimetric or micrometric sized particles, the use of nanofluids will mitigate the problem of flow path abrasion, rapid particle sedimentation, and equipment clogging. However, there are still penalties like pressure drop and increase in pumping power requirement. The addition of nanoparticles to heat transfer fluids increases the viscosity of the fluids which is why the penalty of pressure drop and increased pump power is still of major concern. Peng et al. [3] established that frictional pressure drop of nanorefrigerant (refrigerant-based nanofluid) flowing in horizontal smooth tube is higher when compared to the base fluid refrigerant, and it increases with the increase of volume fraction of the nanoparticles dispersed. In a more recent work by Alawi et al.

[4], they showed that viscosity and pressure drop of nanorefrigerant in pipe flow increase with increase in nanoparticles volume fractions and predicted the viscosity of the nanorefrigerant using Brinkman model [5]. However, researchers like Mahbulul et al. [6, 7] and Murshed et al. [8] maintained that the classical models based on Einstein's [9] equation of suspension viscosity such as Mooney [10] and Brinkman [5] models used in predicting the viscosity of nanofluids are inapt. Therefore, the rheological behavior of nanofluids including viscosity needs to be evaluated experimentally before implementation in industrial heat recovery and cooling systems.

Some of the other thermophysical properties of nanofluids that are directly or indirectly related to its efficient implementation in heat transfer systems are the electrical conductivity and pH. Electrical conductivity and pH of nanofluids are two interrelated properties that affect the viscosity and the stability of nanofluids [11, 12]. Nevertheless, there are still very limited experimental investigations of these two properties of nanofluids with respect to the effect of volume fraction, temperature change, particle size and dispersion energy.

According to Wong and Kurma [13] evaluating the electrical conductivity of nanofluids would give better understanding about the transport properties of the heat transfer fluids. Particle surface electroneutrality is a situation where the effect of both positive and negative ion concentration cancel out thereby, leaving the particle with zero charge, a condition known as isoelectric point (IEP). The pH at this happen is called pH_{IEP} . When the pH of the suspension is changed the differences $\Delta pH = pH - pH_{IEP}$ and $\Delta pOH = pOH - pOH_{IEP}$ alongside with the concentration of the background electrolyte determine the electrical double layer (EDL) [12]. The higher the difference between the pH and pH_{IEP} (i.e. ΔpH) the higher the viscosity due to higher electroviscous effect resulting from increased EDL size. For a properly homogenous suspension where the effect of aggregation can be assumed minimal, the viscosity of the suspension is higher than the viscosity of the fluid base as a result of two main contributions. Firstly, the dispersion of particles increase the rate of energy dissipation due to the distortion of the flow and ionic fields surrounding the particles. Secondly, the change in the EDL surrounding the particles gives an additional increase in energy dissipation especially due to the overlapping of EDLs.

The objective of this work is to experimentally investigate the influence of temperature, volume fraction and dispersion energy on the viscosity, electrical conductivity and pH of SiO_2 -ethylene glycol nanofluids. There is currently a single work done on this nanofluid regarding its effective viscosity [14] and the said work does not consider the influence of temperature and energy of dispersion. There is no known publication on the electrical conductivity of SiO_2 -ethylene glycol nanofluid and many reported work done on the pH of nanofluids (SiO_2 -ethylene glycol not inclusive) were carried out at room temperature (they assumed that temperature does not influence the pH of nanofluids). Since nanofluids are meant for high temperature processes (e.g. in heat exchangers) it is expedient

to understand how temperature increase may affect the pH nanofluids.

EXPERIMENTAL

Materials

The silicon oxide was supplied as white powder from Nano Amorphous Inc. The material came with 99.5% purity and was used with further purification. As stated by Gustafsson et al. [15], attempts on further purification of nanopowder may lead to contamination. Transmission electron microscopy (JEOL JEM-2100F) showed that the nanoparticles are roughly spherical with an average particle diameter of 13.4 ± 5.6 nm (Figure 1) from size analysis. The true density of the nanoparticle is between 2.17 - 2.66 g/cm³. The ethylene glycol used was obtained from Merck with 99.5% purity, viscosity of 16.9 at 25°C and pH between 6-7.5. It is noteworthy to say that all materials and chemicals are of analytical grade.

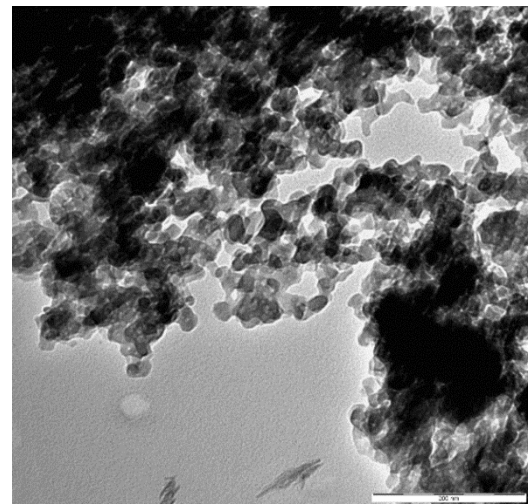


Figure 1 Transmission electron microscope image of SiO_2 nanoparticles

Equipment and methods

The weight of the nanoparticles and base fluid was measured using RADWAG precision balance (AS 220.R2) to prepare a predetermined volume fraction. The prepared samples were sonicated using Q700 ultrasonicator (Qsonica, USA) equipped to measure the total energy impacted into the dispersion process. The size and morphology characterization were carried out using transmission electron microscope (TEM). The nanoparticles were dispersed in acetone so that rapid drying method could be employed (Wamkam *et al* 2011) for the TEM captures. X-Ray Diffraction (XRD) patterns of the nanoparticle samples were obtained using XPERT-PRO X-Ray Diffractometer manufactured by PANalytical BV, Netherlands. The shear viscosity of the nanofluid samples was measured using SV-10 vibro-viscosimeter. The working temperature was between 20–70°C and this was accomplished with the use of constant temperature thermal bath (Lauda Eco Silver RE1225). The pH and electrical conductivity were measured using Jenway 3510 pH meter with -2-19.999 pH measurement

range and EUTECH CON700 electrical conductivity meter respectively. More details on the experimental procedure can be found elsewhere [11].

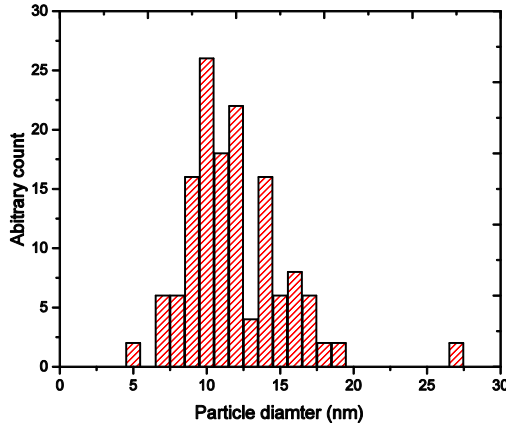


Figure 2 Size analysis of SiO₂ nanoparticles (13.4±5.6 nm)

THEORY

The dynamic viscosity of a dilute colloidal suspension μ is higher than that of the suspending medium μ_o . This was theoretically expressed as in equation (1) by Einstein.

$$\mu = \mu_o(1 + [\eta]\phi) \quad (1)$$

where ϕ is the volume fraction of the particles in suspension, $[\eta]$ in the equation is the intrinsic viscosity taken as 2.5 for uncharged, hard, spherical particle. However, the value may be higher for other geometries [17]. Several models have been proposed to either consider the particle-particle interaction or to extend the Einstein model beyond the dilute regime [5, 10, 18]. According to researcher like Smoluchowski [17] and Booth [19], increase in suspension viscosity is as a results of not only the energy dissipation resulting from flow and EDL disruption around the suspended particles but a major contribution from secondary electroviscous effect due to the overlapping interaction of EDL. This effects has been grouped into a single model equation [20];

$$\mu = \mu_o(1 + [\eta](1 + p)\phi + \mathcal{G}(\phi^2)) \quad (2)$$

Here p stands for the coefficient of primary electroviscous effect as a results of shear distortion of the EDL surrounding a charged particle and \mathcal{G} is the coefficient of secondary electroviscous effect (and it is synonymous to Huggin's coefficient elsewhere [18]) due to the interaction of EDL involving at least two particles. For a very small particle having EDL thickness of the same magnitude as the radius of the particle, the primary electroviscous effects become very dominant [21]. In this case equation (2) becomes;

$$\mu = \mu_o(1 + [\eta](1 + p)\phi) \quad (3)$$

The primary electroviscous effect p was later expressed by Adachi et al. [22] as;

$$p = \frac{(a + \kappa^{-1})^3 - a^3}{a^3} \quad (4)$$

In the above equation a is the radius of the particle, κ^{-1} is the thickness of the EDL and it is also known as Debye length. The secondary electroviscous effect \mathcal{G} may not be much of significance when the particle concentration is lower than 10% as particle-particle interactions primarily occur at higher volume fractions [23]. In order to evaluate p , the EDL thickness must be evaluated for the Debye length give as;

$$\kappa^{-1} = \sqrt{\frac{\epsilon_0 \epsilon_r k_B T}{2 N_A e^2 I}} \quad (5)$$

where k_B is the Boltzmann constant, T is the absolute temperature taken as 300°K, ϵ_0 is the permittivity of the vacuum give as $8.854 \times 10^{-12} \text{ C}^2 \cdot \text{N}^{-1} \cdot \text{m}^{-2}$, ϵ_r is the dielectric constant for the suspending medium (ethylene glycol = 37.7), N_A is the Avogadro's number, e is the charge and I is the ionic strength (moles/m³). To evaluate the ionic strength of the suspension a procedure was suggested by Rubio-Hernández et al. [12] and had been successfully used by Anoop et al. [23]. The above equations have been derived for cases where the ionic strength of the system have been modified using NaOH, HCl or any other modifier possible.

Ruiz-Reina and Carrique [24] did a theoretical calculation and simulated the electroviscous effect on concentrated colloids in salt-free medium. A case very much like the nanofluid in this experiment where in no NaOH, HCl or the likes are added. The effective viscosity of colloid of this nature was derived to be:

$$\mu = \mu_o \left(1 + \frac{5}{2} \phi S(\phi) \right) \quad (6)$$

And

$$S(\phi) = \frac{4(1 - \phi^{7/3})}{4(1 + \phi^{10/3}) - 25\phi(1 + \phi^{4/3}) + 40\phi^{5/3}} \quad (7)$$

when the nanoparticle concentration is very dilute the function $S(\phi)$ tends to 1 and equation (6) becomes equation (1).

RESULTS

The dynamic viscosity of pure ethylene glycol and ethylene glycol-based nanofluids of SiO₂ were measured from 20°C to 70°C by increment of 5°C per step. The base fluid data compared very well with published data of Xie et al. [25] and Pastoriza-Gallego et al. [26] with less than ±5% deviation (not presented here). Figure 3 shows the influence of temperature on the viscosity of ethylene glycol-SiO₂ nanofluids. The behaviour of the nanofluids is such that the viscosity diminishes exponentially with increase in the fluid temperature. This is typical of nanofluids as widely published in the literature [27].

The trends describing the change in viscosity with temperature is similar for all volume fractions and irrespective of the dispersion energy applied. This results indicate reliability of the trend of the experimental results. Varying the dispersion energy is necessary in the preparation of nanofluids in order to determine the optimum energy required for the preparation at which point the viscosity will be minimum indicating a homogenous dispersion. It is a well-known procedure to use rheology to characterize the state of dispersion of nanomaterials in base fluid [28]. This is an ongoing research work, therefore only two dispersion energies have been investigated and the

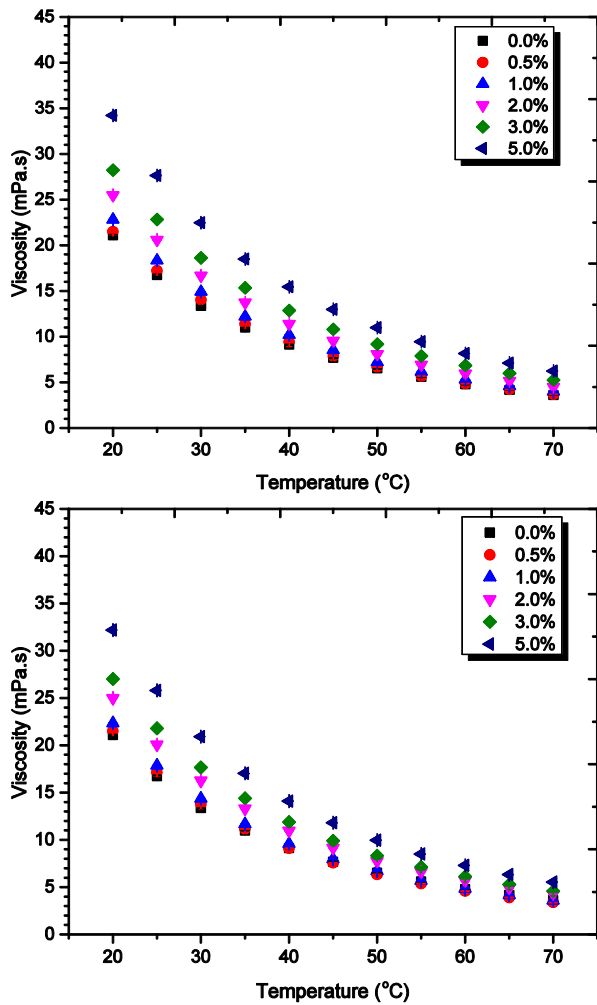


Figure 3 Influence of temperature on the viscosity of ethylene glycol-SiO₂ nanofluid (a) prepared with $1.5 \times 10^5 \text{ kJ/m}^3$ dispersion energy (b) prepared with $3.2 \times 10^5 \text{ kJ/m}^3$ dispersion energy

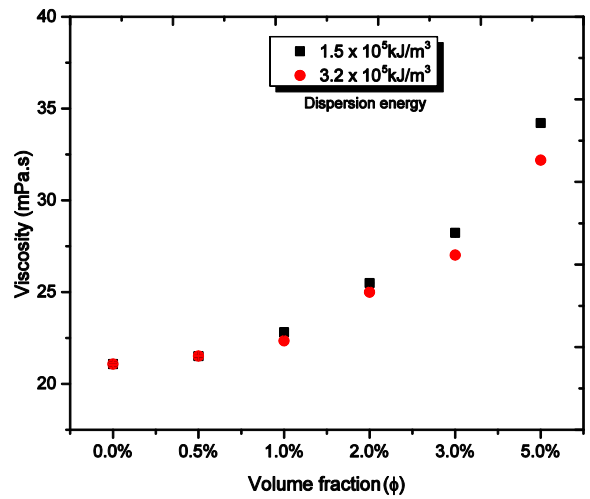


Figure 4 Combined influence of volume fraction and energy density on the viscosity of ethylene glycol-SiO₂ nanofluids

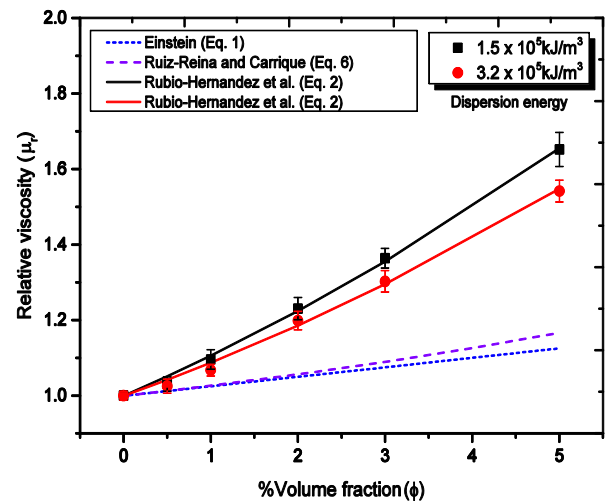


Figure 5 Prediction of experimental relative viscosity at 25°C with Equations (1), (2) and (6).

result is presented in Figure 4. From what it apparent in Figure 4, the nanofluid samples up to 2% volume fraction were consistent in dispersion at the application of $1.5 \times 10^5 \text{ kJ/m}^3$ energy density. Further increment in the energy density showed that the a slight reduction in the value of the viscosity recorded. This reduction at the application of $3.2 \times 10^5 \text{ kJ/m}^3$ energy density is less than 2% at 20°C.

The model of Einstein in equation (1), Rubio-Hernández et al. [20] in equation (2), and Ruiz-Reina and Carrique [24], in equation (6) were all used to predict the viscosity behaviour of the nanofluids in the present experimental study as shown in Figure 5. Both the Einstein, and Ruiz-Reina and Carrique under predicted the present experimental data. Using nonlinear regression code and running maximum of 200 iterations, equation (6) fitted the present experimental data with very good agreement. The p and ϑ in the equation (2) are -0.9601 and 0.0063 for $1.5 \times 10^5 \text{ kJ/m}^3$ energy density. While for $3.2 \times 10^5 \text{ kJ/m}^3$ energy density p and ϑ are -0.9673 and 0.0056 respectively.

The pH and electrical conductivity of the base fluid showed a virtually unchanging value with respect to the temperature increment. Pure ethylene glycol is poor at ionization due to its mild polarity [29] which is the primary cause of the behaviour observed. The addition of SiO₂ nanoparticles showed significant jumps in both the electrical conductivity and the pH of the suspension. The influence of temperature increment on the electrical conductivity is corresponding increment across all the volume fraction investigated as presented in Figure 5(a). It is seen that the electrical conductivity of the silica nanofluids increase linearly with increase in the temperature. However, Figure 5(b) shows that the pH of the suspension reduced with increase in temperature of the nanofluid. This trend is typical of pH of nanofluids based on other published works [11, 30].

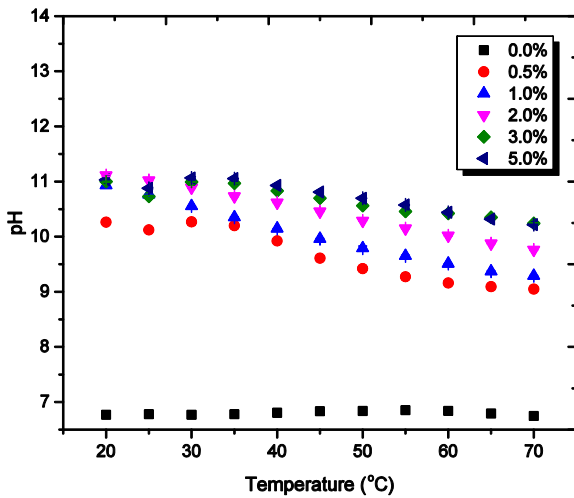
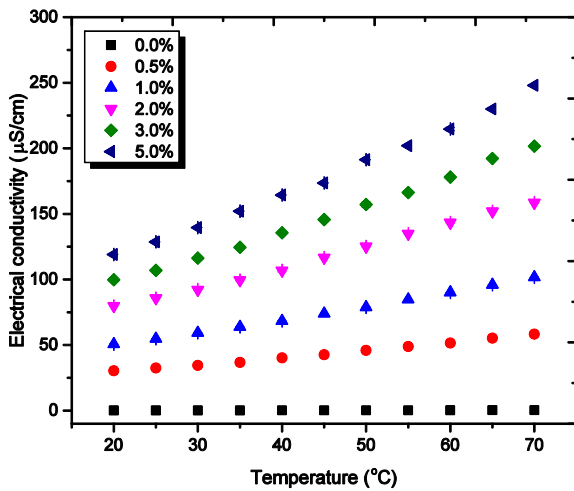


Figure 5 Effect of temperature increment on the electrical conductivity and pH of ethylene glycol-SiO₂ nanofluids (a) electrical conductivity (b) pH

The influence of increasing volume fraction on the both the electrical conductivity and pH is presented in Figure 6. It was observed that the electrical conductivity of the SiO₂ nanofluids increased with increase in volume fraction. However, the increment is nonlinear which depicted the occurrence of counterion condensation. A situation where there is saturation of opposite ion on the nanoparticles and further increment does not show a corresponding increment in electrical conductivity. At this point the electrical conductivity will sometimes reduce until a plateau is formed [31].

Interestingly, the pH of the nanofluids also showed increment in values with regards to increment of the volume fraction. It further showed a plateau in pH value irrespective of the volume fraction and the plateau corresponds with point where counterion condensation sets in the electrical conductivity measurements. On the effect of the energy of suspension, about 6% reduction in the electrical conductivity was observed and approximately 3.5% reduction in pH value at 5% volume fraction was observed.

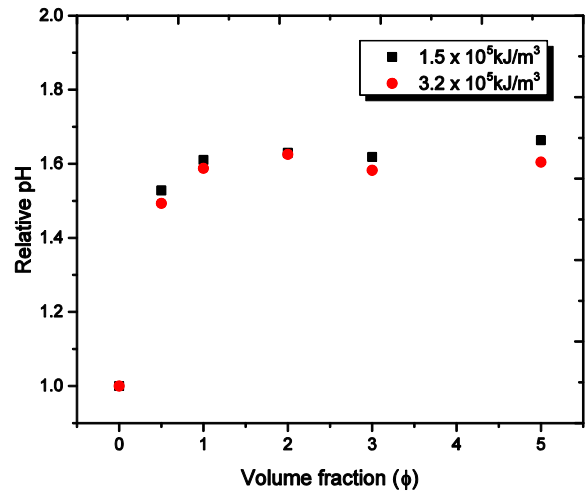
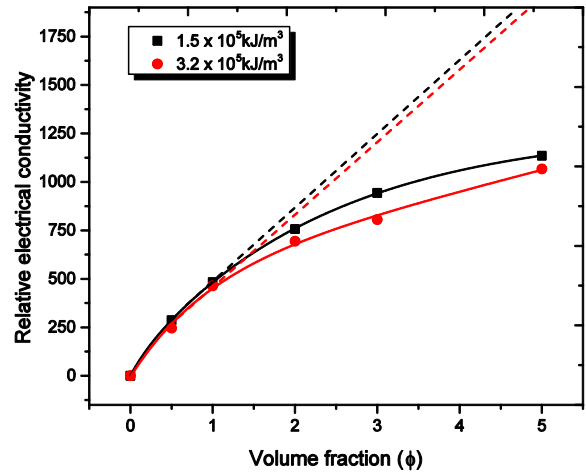


Figure 6 Influence of viscosity on electrical conductivity and pH of ethylene glycol-SiO₂ nanofluid (a) electrical conductivity, the dotted lines depict when counterion condensation effect is neglected (b) pH

CONCLUSION

In the present work experimental investigations was carried out on the thermophysical properties of SiO₂-ethylene glycol nanofluids, namely; viscosity, pH and electrical conductivity. The factors investigated were particle volume fraction, temperature and energy of dispersion. Based on the results, it was clear that all the thermophysical properties investigated are influenced by change in volume fraction and temperature. Within the confines of the energy densities investigated a 2% deviation in relative viscosity value was recorded, 6% relative electrical conductivity deviation and 3.5% relative pH deviation.

REFERENCES

- [1] Maxwell J.C., *Electricity and Magnetism*, (Oxford, Clarendon, 1873)
- [2] Choi S., and Eastman J., Enhancing thermal conductivity of fluids with nanoparticles, in *ASME Int. Mech. Eng. Congr. Expo.*, San Francisco, CA, 1995)

- [3] Peng H., Ding G., Jiang W., Hu H., and Gao Y., Measurement and correlation of frictional pressure drop of refrigerant-based nanofluid flow boiling inside a horizontal smooth tube, *Int. J. Refrig.*, Vol. 32, 2009, pp. 1756–1764
- [4] Alawi O.A., Azwadi N., Sidik C., and Kherbeet A.S., Measurements and correlations of frictional pressure drop of TiO₂/R123 flow boiling inside a horizontal smooth tube ☆, *Int. Commun. Heat Mass Transf.*, Vol. 61, 2015, pp. 42–48
- [5] Brinkman H.C., The viscosity of concentrated suspensions and solutions, *J. Chem. Phys.*, Vol. 20, 1952, pp. 571
- [6] Mahbulul I.M., Saidur R., and Amalina M. a., Influence of particle concentration and temperature on thermal conductivity and viscosity of Al₂O₃/R141b nanorefrigerant, *Int. Commun. Heat Mass Transf.*, Vol. 43, 2013, pp. 100–104
- [7] Mahbulul I.M., Khaleduzzaman S.S., Saidur R., and Amalina M. A., Rheological behavior of Al₂O₃/R141b nanorefrigerant, *Int. J. Heat Mass Transf.*, Vol. 73, 2014, pp. 118–123
- [8]vMurshed S.M.S., Leong K.C., and Yang C., Thermophysical and electrokinetic properties of nanofluids - A critical review, *Appl. Therm. Eng.*, Vol. 28, 2008, pp. 2109–2125
- [9]vEinstein A., A New Determination of Molecular Dimensions, *Ann. Phys.*, Vol. 4, 1906, pp. 37–62
- [10]vMooney M., The viscosity of a concentrated suspension of spherical particles, *J. Colloid Sci.*, 1951, pp. 3–4
- [11] Adio S.A., Sharifpur M., and Meyer J.P., Investigation into the Effective Viscosity, Electrical Conductivity and pH of g-Al₂O₃-Glycerol nanofluids in Einstein Concentration Regime, *Heat Transf. Eng.*, Vol. 36, 2015,
- [12] Rubio-Hernández F.J., Ayúcar-Rubio M.F., Vlaázquez-Navarro J.F., and Galindo-Rosales F.J., Intrinsic viscosity of SiO₂, Al₂O₃ and TiO₂ aqueous suspensions, *J. Colloid Interface Sci.*, Vol. 298, 2006, pp. 967–972
- [13] Wong K.-F.V., and Kurma T., Transport properties of alumina nanofluids, *Nanotechnology*, Vol. 19, 2008, pp. 345702
- [14] Rudyak V.Y., Dimov S. V., Kuznetsov V. V., and Bardakhanov S.P., Measurement of the viscosity coefficient of an ethylene glycol-based nanofluid with silicon-dioxide particles, *Dokl. Phys.*, Vol. 58, 2013, pp. 173–176
- [15] Gustafsson J., Mikkola P., Jokinen M., and Rosenholm J.B., The influence of pH and NaCl on the zeta potential and rheology of anatase dispersions, *Colloids Surfaces A Physicochem. Eng. Asp.*, Vol. 175, 2000, pp. 349–359
- [16] Wankam C.T., Opoku M.K., Hong H., and Smith P., Effects of pH on heat transfer nanofluids containing ZrO₂ and TiO₂ nanoparticles, *J. Appl. Phys.*, Vol. 109, 2011, pp. 024305
- [17] Smoluchowski M. V., Theoretische Bemerkungen über die Viskosität der Kolloide, *Kolloidzshr*, Vol. 80, 1916, pp. 190–195
- [18] Krieger I., and Dougherty T., A mechanics for non-Newtonian flow in suspensions of rigid spheres, *Trans. Soc. Rheol.*, Vol. 3, 1959, pp. 137–152
- [19] Booth F., The electroviscous effect for suspensions of solid spherical particles, *Proc. R. Soc. A Math. Phys. Eng. Sci.*, Vol. 203, 1950, pp. 533–551
- [20] Rubio-Hernández F.J., Gómez-Merino a I., Ruiz-Reina E., and García-Sánchez P., An experimental test of Booth's primary electroviscous effect theory., *J. Colloid Interface Sci.*, Vol. 255, 2002, pp. 208–213
- [21] Honig E., Pünt W.F., and Offermans P.H., The primary electroviscous effect: Measurements on silica sols, *J. Colloid Interface Sci.*, Vol. 134, 1990, pp. 169–173
- [22] Adachi Y., Nakaishi K., and Tamaki M., The viscosity of a dilute suspension of sodium montmorillonite in an alkaline state, *Colloids Surfaces A Physicochem. Eng. Asp.*, Vol. 131, 1998, pp. 69–75
- [23] Anoop K.B., Kabelac S., Sundararajan T., and Das S.K., Rheological and flow characteristics of nanofluids: Influence of electroviscous effects and particle agglomeration, *J. Appl. Phys.*, Vol. 106, 2009, pp. 034909 1–7
- [24] Ruiz-reina E., Electroviscous Effect of Concentrated Colloidal Suspensions in Salt-Free Solutions, 2007, pp. 141–148
- [25] Xie H., Yu W., and Chen W., MgO nanofluids: higher thermal conductivity and lower viscosity among ethylene glycol-based nanofluids containing oxide nanoparticles, *J. Exp. Nanosci.*, Vol. 5, 2010, pp. 463–472
- [26] Pastoriza-Gallego M.J., Lugo L., Legido J.L., and Piñeiro M.M., Thermal conductivity and viscosity measurements of ethylene glycol-based Al₂O₃ nanofluids., *Nanoscale Res. Lett.*, Vol. 6, 2011, pp. 221–231
- [27] Namburu P.K., Kulkarni D.P., Misra D., and Das D.K., Viscosity of copper oxide nanoparticles dispersed in ethylene glycol and water mixture, *Exp. Therm. Fluid Sci.*, Vol. 32, 2007, pp. 397–402
- [28] Song Y.S., and Youn J.R., Influence of dispersion states of carbon nanotubes on physical properties of epoxy nanocomposites, *Carbon N. Y.*, Vol. 43, 2005, pp. 1378–1385
- [29] Sarojini K.G.K., Manoj S. V., Singh P.K., Pradeep T., and Das S.K., Electrical conductivity of ceramic and metallic nanofluids, *Colloids Surfaces A Physicochem. Eng. Asp.*, Vol. 417, 2013, pp. 39–46
- [30] Konakanchi H., Vajjha R.S., Chukwu G. a., and Das D.K., Measurements of pH of Three Nanofluids and Development of New Correlations, *Heat Transf. Eng.*, Vol. 36, 2014, pp. 81–90
- [31] White S.B., Shih A.J., and Pipe K.P., Investigation of the electrical conductivity of propylene glycol-based ZnO nanofluids, *Nanoscale Res. Lett.*, Vol. 6, 2011, pp. 346–350

A NEW METHOD FOR SIMULATING THE CONVECTIVE HEAT TRANSFER OF SUBCRITICAL AND SUPERCRITICAL FLUIDS IN NANOCHANNELS

Gu Y. W., Ge S., Chen M. *

*Author for correspondence

Department of Engineering Mechanics,
Tsinghua University,
Beijing, 100084,
P. R. China

E-mail: mchen@tsinghua.edu.cn

ABSTRACT

In molecular dynamics simulation of convective heat transfer, external driving force and periodic boundary condition are applied to form steady flow. This may induce the temperature fluctuations of fluid at the inlet and unrealistic axial heat conduction at the outlet. In this paper, we propose a new method by inserting/deleting atoms at a given frequency in the region of particle source/sink. Temperature of inlet fluid and walls are then controlled at different values. Compared with previous methods with external driving force and periodic boundary, temperature of inlet fluid can be better up to the desired value while the unrealistic outlet axial conduction has been eliminated. We further simulate convective heat transfer of subcritical and supercritical fluids in nano-channels with this method. Characteristics of fluid flux, temperature, number density are described in detail. The results show that local heat transfer coefficient and Nusselt number increases when there is a transition of fluid state from the subcritical to the supercritical, which is not owing to temperature oscillation at near or supercritical state but an increase of thermal conductivity in the fluid.

INTRODUCTION

Many chemical and biological processes have been designed to take place in nano-fluidic systems over the past decade [1-2]. As these systems have length scales compared to diffusion lengths of nano-particles and molecular size, the thermal control and heat dissipation are technically imperative to ensure their performance and life span. Extensive research has been conducted to understand the process of convective heat transfer in micro- and nano- channels during the last decade. Experimentally, single-phase microscale heat sinks

made from different materials have been tested and proved efficiently to cool electronics [3-5]. Computationally, numerical simulations have been designed to find the truths which affect the momentum and heat transfer in fluid flow [6-8]. In micro- and nano-channels, interface properties such as surface roughness, fluid-wall interactions dominate in the convective heat transfer for liquid flows [9] while rarefaction effect stands out for gaseous flows [10]. Characteristics of fluid flow and heat transfer in such channels behave significantly different. Since the direct measurement by experiments is difficult to accomplish in the channel of hydraulic diameter lower than 100 nm [11], investigations on the convective heat transfer are often performed by the direct simulation Monte Carlo (DSMC) [12] and molecular dynamics simulation (MDS) [13, 14].

In molecular dynamics simulation of convective heat transfer, one popular method is that an external driving force is imposed only to inlet atoms and these atoms press the rest of the fluid. Periodic boundary condition is applied to form steady flow [13]. The problems exist at the channel inlet and outlet [15]. The temperature of inlet fluid deviates from the desired value because the external force is applied after the region of temperature reset and it adds kinetic energy of inlet fluid. One solution is that positions of two regions are exchanged, but the inlet temperature still depends on the magnitude of force and width of both regions [14]. Another problem is that unrealistic axial heat conduction emerges at the outlet, which is caused by temperature difference between outlet atoms and images of inlet atoms under the periodic boundary [16]. A probable solution to this problem is to develop an effective outflow model, in which the outlet temperature field is obtained through

iteration of upstream temperature of fluid. Since problems are induced by external driving force and periodic boundary, it would be better to resort to a method without these conditions.

In this study, we present a new method to simulate convective heat transfer in molecular dynamics. Two regions of particle source/sink are located at both ends of the nano-channel. Steps are conducted to insert particles at the region of source and delete the same amount of particles at the region of sink, which is used to form steady flow instead of periodic boundary. The frequency of inserting or deleting atoms determines the velocity of flow instead of external driving force. With this method, we simulate the convective heat transfer to near-critical fluids. Since the thermo-physical properties of fluid near the critical state change rapidly, the convective heat transfer turns out new features. Many researchers found that the free convection heat transfer coefficients of fluid at the near-critical state were quite high [17]. Another experimental phenomenon at the macro-scale is that pressure and temperature oscillations may exist with the time of observation [18]. It is still unknown for us whether these conclusions are invalid in micro- and nano-channels or not. Therefore, we study the characteristics of fluid flux, density and temperature distributions near the critical state in nano-channels. Variations of local heat transfer coefficients and Nusselt numbers are also discussed in detail.

SIMULATION METHOD

Simulations have been performed on a unary system in LAMMPS [19] containing three different regions, as shown in Figure 1. Two controlled regions, particle source/sink, are located at each end of the system and each region is surrounded by the reflective walls in x and y directions. In the region of particle source, atoms will be inserted by searching voids among existing atoms according to a setting frequency (time interval). The radius of voids should be at least larger than the size of one atom, which guarantees the success of inserting. In the region of particle sink, the same amount of atoms will be deleted at the same frequency of inserting. After many steps, the fluid flow in middle region can reach a steady state. By control the temperatures of inlet fluid and solid walls, we can simulate the process of convective heat transfer.

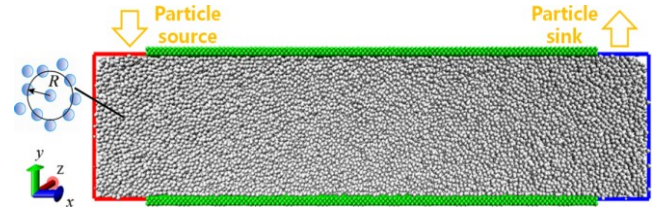


Figure 1 Schematic of MD simulation of particle source/sink method

The system consists of 112,710 Argon atoms and 36,180 wall atoms, corresponding to a size of $450 \times 120 \times 120 \text{ \AA}^3$ in x , y , z direction. Wall atoms employ the Argon and are connected to FCC (001) lattice sites using harmonic springs with the lattice constant $a = 4 \text{ \AA}$ and a spring constant $k = 70 \text{ N/m}$ [8]. The interactions among all atoms are modeled using the 12-6 Lennard-Jones potential:

$$u(r) = 4\epsilon \left[\left(\frac{\sigma}{r} \right)^{12} - \left(\frac{\sigma}{r} \right)^6 \right] \quad (1)$$

where $u(r)$ is the potential energy, r is the distance between two interplay atoms, σ and ϵ represent the low-speed collision diameter and the depth of potential well. For the fluid-fluid interaction, $\sigma_{\text{Ar-Ar}} = 3.405 \text{ \AA}$ and $\epsilon_{\text{Ar-Ar}} = 1.67 \times 10^{-21} \text{ J}$ [20]; For the fluid-wall interaction, $\sigma_{\text{Ar-wall}} = 3.405 \text{ \AA}$ and $\epsilon_{\text{Ar-wall}}$ is varied to adjust the interface wettability. The cutoff radius is set as $R_{\text{cut}} = 10 \text{ \AA}$ and atoms out of R_{cut} have no interactions with one at the inner range. Periodic boundary is only applied to z direction. The time interval to insert or delete an atom is 10 fs, which results in the average velocity of fluid about 43 m/s when the interface wettability is $\epsilon_{\text{fw}} / \epsilon_{\text{ff}} = 1.0$. In order to simulate the convective heat transfer, each inserting atom will be assigned a thermal velocity at random under the desired inlet temperature while the walls are controlled at a different temperature by the Nosé-Hoover thermostat with temperature damping parameter 100 fs as recommended in Ref. 19. The time step is 1 fs and each case of simulations lasts 8 ns. The system is relaxed for up to 2 ns to reach steady flow before the calculation starts.

RESULTS AND DISCUSSION

Validation of the New Method

In the validation procedure, temperature of inlet fluid is set at $T_{in} = 200$ K and the wall temperature is controlled at $T_w = 300$ K, corresponding to the supercritical fluid. In Figure 2 and Figure 3, the results of the particle source/sink method are compared with previous methods with external driving force and periodic boundary. Figure 2 shows that temperature of inlet fluid deviates from 200 K in the original method with external driving force [13] while this deviation is not obvious in this method. This is due to the external driving force that adds kinetic energy of inlet fluid. The temperature of inlet fluid is better up to the desired value with the particle source/sink method.

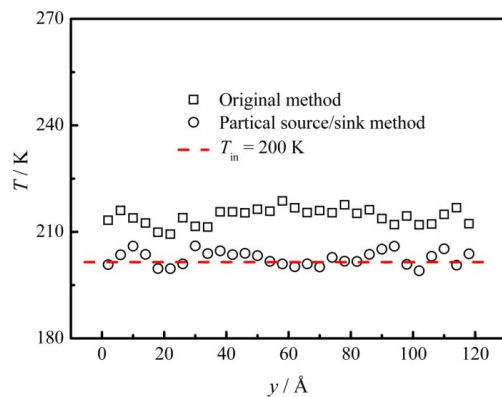


Figure 2 Temperature of inlet supercritical fluid

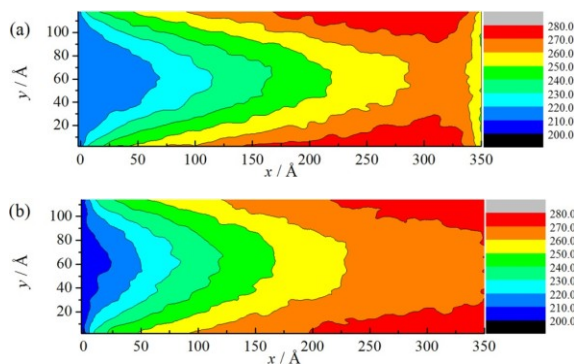


Figure 3 Temperature distribution in the channel: (a) original method with periodic boundary in Ref. 13 and 14; (b) particle source/sink method

When periodic boundary is applied, downstream images of inlet atoms will affect outlet atoms that leads to unrealistic axial heat conduction when there is a temperature difference. This phenomenon exists in both Ref. 13 and 14 as demonstrated in Figure 3(a). From Figure 3(b), it can be seen that this unrealistic axial conduction has been eliminated in the particle source/sink method without periodic boundary. The supercritical fluid is heated gradually by the hot walls without the interruption of images of cold inlet atoms.

Convective Heat Transfer to Near-Critical Fluids

The simulations are then carried out with Argon at the near-critical state. Temperature of inlet fluid is set at $T_{in} = 120$ K and the wall temperatures are controlled at the range of 140 K to 180 K, which corresponds to a transition of fluid state from the subcritical to the supercritical. Figure 4 shows the process of transition in the phase diagram of Argon. The vapor-liquid coexistence curve is obtained from the study of Lennard-Jones fluid system [21]. Three different interface wettabilities are adopted: $\epsilon_{fw} / \epsilon_{ff} = 0.5, 1.0$ and 1.5 , where the contact angle changes from 90° to 0° . It is worth noting that the bulk fluid density will be influenced by the interface wettability. A decrease in the bulk density happens at the more wettable surface while an increase happens at the less wettable surface at the same temperature of fluid [22, 23]. The density shown in Figure 4 is the average value in the whole channel.

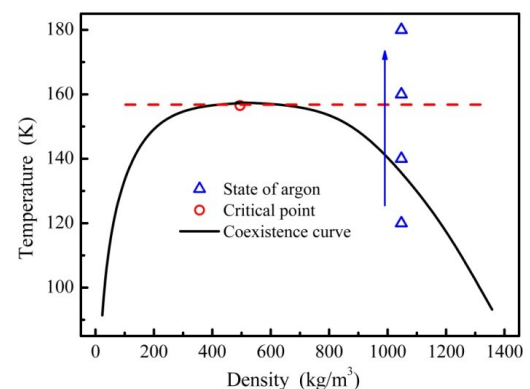


Figure 4 Temperature distribution in the channel: (a) original method with periodic boundary in Ref. 13 and 14; (b) particle source/sink method

Figure 5 shows the variations of mole flux, local average temperature of fluid and number density along the flow direction. In the region of particle source, the flux increases linearly, corresponding to a uniform particle distribution. It is seen that the flow rate approaches a constant in the middle region, which means that the systems reaches a steady state. The local average temperature of fluid increases with increasing wall temperature while the number density decreases gradually. At the near-critical state, the number density undergoes an obvious drop, which represents a transition from sub-critical liquid to supercritical fluid. The flux also undergoes a small fluctuation. These changes are consistent with the observed phenomenon of near-critical water [17]. Besides, there is no obvious temperature oscillation at the near-critical state during our simulation.

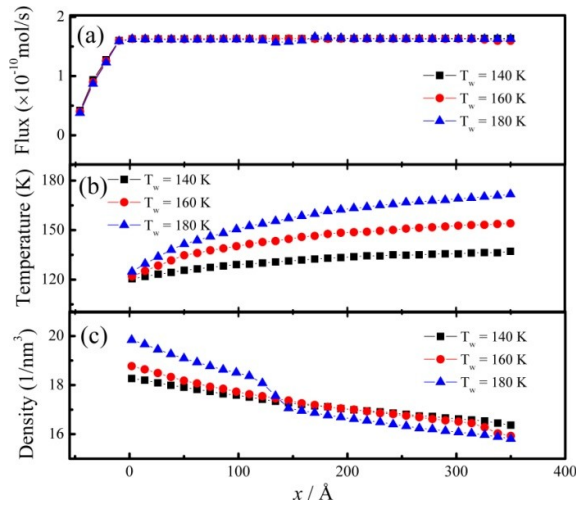


Figure 5 Local average flux, temperature, density of fluid

Although there are some defects to simulate convective heat transfer under periodic boundary in previous literatures, studies have shown confidently more heat can be transferred in the case of an attractive fluid-wall interaction than in the case of a repulsive interaction with increasing pressure drop [13]. Experiments also referred that the heat transfer coefficient of water in the hydrophilic micro-channels was higher than that in the hydrophobic channels [24]. As shown in Figure 6(a), our results with the method of particle source/sink demonstrate that outlet temperature of fluid at the case of $\varepsilon_{fw} / \varepsilon_{ff} = 1.5$ is higher than that of other two channels at the same frequency of inserting/deleting atoms, owing to lower thermal resistance at

the more wettable surface [25]. Since the fluid is heated with a transition of sub-critical liquid to supercritical fluid (120 K to 180 K), there is an obvious density drop in the Figure 6(b) and 6(c), which corresponds to a large density gradient near the critical state. However, it cannot be seen at the less wettable channel (Figure 6(a)) because the fluid does not reach the critical state. As the surface turns to be more wettable, it can be induced that more heat is transferred to accelerate the process of transition with the same fluid velocity.

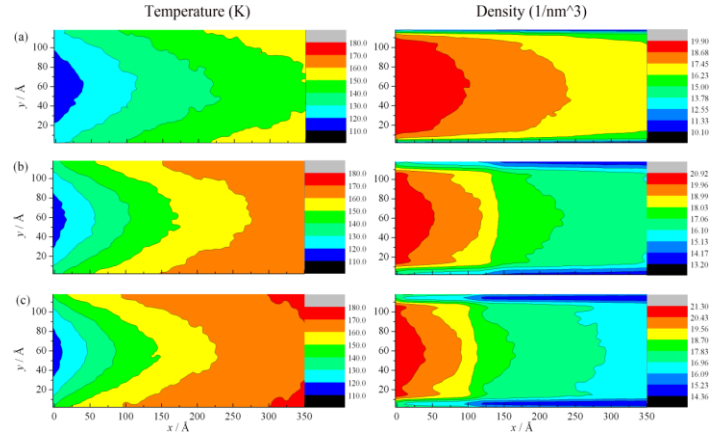


Figure 6 Temperature and density distribution of fluid in the channel: (a) $\varepsilon_{fw} / \varepsilon_{ff} = 0.5$; (b) $\varepsilon_{fw} / \varepsilon_{ff} = 1.0$; (c) $\varepsilon_{fw} / \varepsilon_{ff} = 1.5$

For the process of convective heat transfer, the most concern is the magnitude of heat transfer coefficient, which can be also expressed by the dimensionless temperature gradient, Nusselt number (Nu). Local heat transfer coefficient can be calculated from the energy balance and Nusselt number is determined by:

$$h \cdot (T_w - T_b) = \lambda \left. \frac{\partial T}{\partial y} \right|_{y=0} \quad (2)$$

$$Nu = \frac{hL}{\lambda} \quad (3)$$

where λ is the thermal conductivity of the fluid; L is twice the channel height, $2H$, which is set as the characteristic length. Combining equation (2) and (3), local Nusselt number will be calculated from temperature difference and local temperature gradient near the wall.

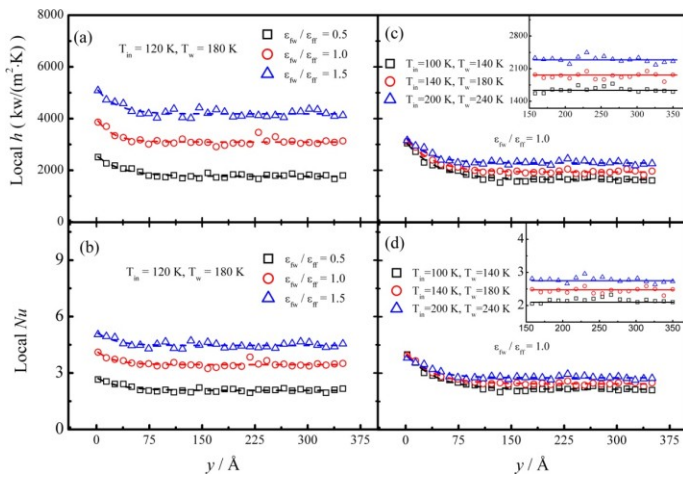


Figure 7 Local heat transfer coefficient and Nusselt number along the flow direction

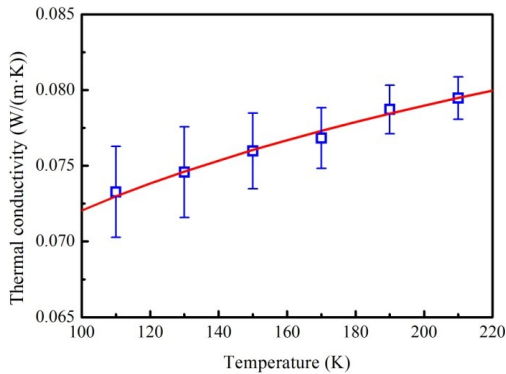


Figure 8 Thermal conductivity of fluid at different temperature of fluid

The calculated results along the flow direction are depicted in Figure 7. In Figure 7(a) and 7(b), the fluid is at near-critical state, $T_{in} = 120$ K and $T_w = 180$ K while three different fluid-wall interactions are presented. It is observed that local heat transfer coefficient and Nusselt number at the more wettable surface are higher than their values at the less wettable surface, which is consistent with previous studies at the periodic boundary [14]. Furthermore, the temperature of inlet fluid and wall are adjusted to make fluid experience three different states at the same channel: subcritical state, $T_{in} = 100$ K and $T_w = 140$ K; near-critical state, $T_{in} = 140$ K and $T_w = 180$ K; supercritical state, $T_{in} = 200$ K and $T_w = 240$ K. Figure 7(c) and 7(d) shows that the local heat transfer coefficient and Nusselt number increases gradually when the thermal state

of fluid changes from subcritical state to supercritical state. The temperature difference between T_{in} and T_w is 40 K, which leads a constant value of $(T_w - T_b)$, about 23 K in all three cases. One possible reason can be due to an increase of thermal conductivity as the temperature of fluid increases in nano-channels as shown in Figure 8. Other variations of properties like viscosity, diffusivity and specific heat etc. may also affect the nanoscale convective heat transfer to near-critical fluids. This will be explored in future work.

CONCLUSION

In summary, we have shown a new method to simulate convective heat transfer in nano-channels without external driving force and periodic boundary. This new method is implied through inserting/deleting atoms at a given frequency in the region of particle source/sink. Temperature of inlet fluid and walls are then controlled at different values. Compared with previous methods with external driving force and periodic boundary, temperature of inlet fluid can be better up to the desired value while the unrealistic outlet axial conduction has been eliminated.

With this method, we further study the characteristics of fluid flux, density and temperature distributions near the critical state in the process of nano-scale convective heat transfer. The results reveal that the local heat transfer coefficient and Nusselt number are not only affected by the interface wettability but also depend on thermal property of fluid at the near-critical state. They increase gradually when the thermal state of fluid changes from subcritical state to supercritical state, which is not owing to temperature oscillation at near or super critical state but an increase of thermal conductivity in the fluid.

ACKNOWLEDGEMENT

This research was supported by the National Basic Research Program of China (Grant No. 2015CB251502) and the Science Fund for Creative Research Groups of National Natural Science Foundation of China (Grant No. 51321002). The computations were carried out at the Tsinghua National Laboratory for Information Science and Technology, China.

REFERENCES

- [1] Pop E., Energy dissipation and transport in nanoscale devices, *Nano Research*, Vol. 3, No. 3, 2010, pp. 147-169.
- [2] Stone H.A., Stroock A.D., and Ajdari A., Engineering flows in small devices: Microfluidics toward a lab-on-a-chip, *Annual Review of Fluid Mechanics*, Vol. 36, 2004, pp. 381-411.
- [3] Hetsroni G., Mosyak A., Pogrebnyak E., and Yarin L.P., Heat transfer in micro-channels: Comparison of experiments with theory and numerical results, *International Journal of Heat and Mass Transfer*, Vol. 48, No. 25, 2005, pp. 5580-5601.
- [4] Morini G.L., Single-phase convective heat transfer in microchannels: A review of experimental results, *International Journal of Thermal Sciences*, Vol. 43, No. 7, 2004, pp. 631-651.
- [5] Hettiarachchi H.D.M., Golubovic M., Worek W.M., and Minkowycz W.J., Three-dimensional laminar slip-flow and heat transfer in a rectangular microchannel with constant wall temperature, *International Journal of Heat and Mass Transfer*, Vol. 51, No. 21, 2008, pp. 5088-5096.
- [6] Chen X., Cao G., Han A., Punyamurtula V.K., Liu L., Culligan P.J., Kim T., and Qiao Y., Nanoscale fluid transport: Size and rate effects, *Nano Letters*, Vol. 8, No. 9, 2008, pp. 2988-2992.
- [7] Wei S., Kakac S., and Yazicioglu A.G., A numerical study of single-phase convective heat transfer in microtubes for slip flow, *International Journal of Thermal Sciences*, Vol. 46, No. 11, 2007, pp. 1084-94.
- [8] Khare R., Keblinski P., and Yethiraj A., Molecular dynamics simulations of heat and momentum transfer at a solid-fluid interface: Relationship between thermal and velocity slip, *International Journal of Heat and Mass Transfer*, Vol. 49, No. 19, 2006, pp. 3401-3407.
- [9] Craighead H.G., Nanoelectromechanical systems, *Science*, Vol. 290, No. 5496, 2000, pp. 1532-1535.
- [10] Gad-El-Hak M., Gas and liquid transport at the microscale, *Heat Transfer Engineering*, Vol. 27, No. 4, 2006, pp. 13-29.
- [11] Pennathur S., and Santiago J.G., Electrokinetic transport in nanochannels. 2. Experiments, *Analytical Chemistry*, Vol. 77, No. 21, 2005, pp. 6782-6789.
- [12] Balaj M., Roohi E., Akhlaghi H., and Myong R.S., Investigation of convective heat transfer through constant wall heat flux micro/nano channels using DSMC, *International Journal of Heat and Mass Transfer*, Vol. 71, 2014, pp. 633-638.
- [13] Markvoort A.J., Hilbers P., and Nedeja S.V., Molecular dynamics study of the influence of wall-gas interactions on heat flow in nanochannels, *Physical Review E*, Vol. 71, No. 06670262, 2005.
- [14] Ge S., Gu Y., and Chen M., A molecular dynamics simulation on the convective heat transfer in nanochannels, *Molecular Physics*, Doi:10.1080/00268976.2014.970593, 2014.
- [15] Alexiadis A., and Kassinos S., Molecular simulation of water in carbon nanotubes, *Chemical Reviews*, Vol. 108, No. 12, 2008, pp. 5014-5034.
- [16] Gu Y., Ge S., and Chen M., A molecular dynamics simulation of nanoscale convective heat transfer with effects of axial heat conduction, *Heat and Mass Transfer*, In press, 2015.
- [17] Pioro I.L., and Duffey R.B., Experimental heat transfer in supercritical water flowing inside channels (survey), *Nuclear Engineering and Design*, Vol. 235, No. 22, 2005, pp. 2407-2430.
- [18] Hines W.S., and Wolf H., Pressure oscillations associated with heat transfer to hydrocarbon fluids at supercritical pressures and temperatures, *Ars Journal*, Vol. 32, No. 3, 1962, pp. 361-366.
- [19] Plimpton S., Fast parallel algorithms for short-range molecular-dynamics, *Journal of Computational Physics*, Vol. 117, No. 1, 1995, pp. 1-19.
- [20] Rowley L.A., Nicholson D., and Parsonage N.G., Monte-carlo grand canonical ensemble calculation in a gas-liquid transition region for 12-6 argon, *Journal of Computational Physics*, Vol. 17, No. 4, 1975, pp. 401-414.
- [21] Al-Matar A.K., Tobgy A.H., and Suleiman I.A., The phase diagram of the Lennard-Jones fluid using temperature dependent interaction parameters, *Molecular Simulation*, Vol. 34, No. 3, 2008, pp. 289-294.
- [22] Nagayama G., and Cheng P., Effects of interface wettability on microscale flow by molecular dynamics simulation, *International Journal of Heat and Mass Transfer*, Vol. 47, No. 3, 2004, pp. 501-513.
- [23] Thomas J.A., and McGaughey A.J.H., Effect of surface wettability on liquid density, structure, and diffusion near a solid surface, *Journal of Chemical Physics*, Vol. 126, No. 0347073, 2007
- [24] Wu H.Y., and Cheng P., An experimental study of convective heat transfer in silicon microchannels with different surface conditions, *International Journal of Heat and Mass Transfer*, Vol. 46, No. 14, 2003, pp. 2547-2556.
- [25] Ge S., and Chen M., Temperature dependence of thermal resistance at a solid/liquid interface, *Molecular Physics*, Vol. 111, No. 7, 2013, pp. 903-908.

Investigation on Ultrasonic Energy Density Effect on Characterization of Zinc Oxide (ZnO) NanoParticle Size Distribution with Using Zeta-Sizer

Sharifpur* M, Ghodsinezhad H, Meyer J.P and Rolfes H
 Department of Mechanical and Aeronautical Engineering,
 Department of Chemical Engineering,
 University of Pretoria,
 Pretoria, 0002,
 South Africa,

*Author for correspondence

E-mail: mohsen.sharifpur@up.ac.za

ABSTRACT

Two-step preparation of nanofluids by using sonication is one of the common ways to prepare nanofluids. Therefore, the nanoparticles supply in the form of ultra-fine powder which inherently aggregated and they need to be broken down by using agitation method. Nevertheless, there is no standard way to indicate what optimum amount of energy density should be used to break down aggregation of exact nanoparticles in specific based fluid. In this on-going research, Zinc Oxide (ZnO) nanoparticles with average size of 20 nm has been supplied and dispersed in deionized water (DI) with using ultrasonic agitation probe. The average particle size has been measured with Malvern Zetasizer to investigate how much sonication energy density is adequate to have minimum mean aggregation size. It has been found energy density $\alpha=3$ KJ/ml given average size of 128 nm for suspension of ZnO with primary size of 20nm in DI water and further sonication couldn't break down aggregation of nanoparticles furthermore, even has got reverse effect on breaking down aggregation size.

INTRODUCTION

Novel advanced heat transfer fluid is called nanofluid by Choi in 1995 [1] which is suspension of nano-size (less than 100nm) metal, non-metal or metal oxide nanoparticles in conventional heat transfer fluids as based fluids. This is to overcome the inherently low thermal conductivity of the based fluids and makes the heat transfer more efficiently. Masuda et al [2] studied concentration of 1.3-4.30 (vol%) Al_2O_3 with particle size 13 nm. They conclude that thermal conductivity of water with could has an increase in the range 10-32%. Eastman et al [3] by adding 0.3 vol% copper nanoparticle with average size of less than 10 nm in Ethylene glycol, the thermal conductivity increases more than 40%. G. Colangelo et al [4] reported thermal conductivity of diathermic oil has an increase of about 3.58% and 8.45% with concentration of 1% and 2% of ZnO (60 nm, primary size), respectively. There are two major methods for preparation of nanofluids, namely single-step method and two-step method.

In single-step method, the nanofluids will be produced physically or in chemical processes that nanoparticles directly have been made and suspended simultaneously into the host fluids (base fluids). Therefore, methods such as vapour condensation[3], chemical vapour deposition[5] and chemical

reduction as well as chemical precipitation [6] could be applied. However, bulk production of single-step method is not cost effective yet and this method also limited to produce nanofluids for low-vapour-pressure of the flowing host fluids. On the other hand, there is not enough reported research on the effect of the time on their stability or their expiry dates.

In order to use nanofluids for an industrial application, large volume of nanofluids as a coolant medium is needed. Therefore, two-step method have implemented by many researchers to produce desired nanofluids by applying different techniques such as magnetic stirrer, high shear homogenizer and ultra-sonication (sonication). Moreover, preparing stable nanofluids is very critical from the Industrial application point of view. Therefore, preparing long time chemically stable nanofluids could be achieved by changing surface characteristics of nanoparticles by using additives. This is with increasing wettability of the surface of particles with surrounded interface fluids as well as large micro molecules prevent particles surface from coming close contact to neighbours particles. In this way it needs to illustrate adequate surfactant which adsorbs on the surface of particles as well as compatibility with based fluids. This must be on the presence of processing fluids (liquid bridge); or enhance electrostatic interaction with adjusting pH value to increase repulsive force within particles [7].

In this research 20 nm ZnO nanoparticles is chosen for preparing the nanofluids by applying two-step method. Actually, the application of ZnO is increasing in different industries due to its unique characteristics. In electronic industry ZnO is used to make semiconductor for making inexpensive transistor and thin film batteries due to abundant, inexpensive and chemically stable [8].

According to the Stoke's law, reducing the size of constituent in a solution cause reducing the rate of sedimentation velocity.

$$v_s = \frac{2}{9} \frac{R^2 (\rho_s - \rho_{BF})}{\mu_{BF}} g \quad (1)$$

where ρ_s and ρ_{BF} are the density of solid nanoparticles and the based fluid, respectively. μ_{BF} is the dynamic viscosity of the based fluid and R is the average radius size of the solid particles in the fluid. Consequently, by reducing average size of

the particles, the rate of sedimentation will be decreased or in other words, stability of the nanofluids will be increased [9]. The average size of suspended nanoparticles as a nanofluid is usually greater than the primary size of the particles which provided by manufacturers.

Chung et al. [10] prepared ZnO-water nanofluids, nanopowders have been purchased from different supplier with various primary size 20nm and 40-100nm. Different sonication methods were used for preparation nanofluids. Bright field TEM and photocorrelation Spectroscopy are used to characterize nanofluids. It was reported that the mean particle size has distribution range 50- 300 nm . From their results applying 60 minutes ultrasonic agitation with horn type ultra-sonicator the average size of 20nm and 40-100 nm are 92 nm and 94 nm respectively. According to them different primary particle size is given similar mean particle size in their base fluids.

Suganthi et al. [11] investigated the effect of temperature on the zeta potential, size distribution and viscosity profile for ZnO (20% of weight) in deionized water by adding sodium hexa metaphosphate as surfactant. They used 35-40 nm nanoparticles, but reported the minimum mean size of 136 nm at 25° C after three hours sonication time (750 W ,20 KHz. 45 seconds pulse on 15 seconds pulse off). They also found as the temperature increases, the hydrodynamic size also increases. This is due to intensifying Brownian motion, therefore, the particle to particle interaction would scale up aggregation.

Suganthi et al. [12] reported 24 hours sonication is needed to break aggregation of ZnO nanoparticles in Ethylene glycol from 200nm to minimum average hydrodynamic size of 100 nm.

Kole et al [13] studied the effect of prolonged sonication of ZnO with primary size of 30-40 nm in Ethylene glycol without any surfactant. They indicated that 60 hours sonication using 200 W sonicator could break down aggregation of nanoparticles approximately about 91 nm (measured with zeta sizer Malvern ZS) while after 4 hours the average size of the nanoparticles in the nanofluid was about 459 nm. Their results show more than 60 hours sonication could increase the average size. For example, 100 hours sonication caused the average size of 220 nm. It has not been specified what was based fluid volume, which has been prepared, to determine sonication energy density.

Wei Yu et al [14] found average size of ZnO (primary size 10-20 nm) in Ethylene glycol vary from 500 nm (after 5 min sonication) to 227nm and 209 nm, after 2h and 4h sonication, respectively.

Table1. summary of preparation nanofluids with sonication

Author	Particle	Based Fluid	additives	Primary size nm	Sonication time min	Min average size nm
Chung et al[10]	ZnO	DI Water	Ammonium polymethacrylate	20	60	92
Chung et al[10]	ZnO	DI Water	Ammonium polymethacrylate	40-100	60	94
K.S. Suganthi et al [11]	ZnO	Water	Sodiumhexa-metaphosphate (SHMP)	35-40	180	136
K.S. Suganthi[12]	ZnO	Ethylene glycol	No- surfactant	25-40	24 x 60	100
Madhusree Kole et al[13]	ZnO	Ethylene glycol	No- surfactant	30-40	60 x 60	91
Wei Yu et al[14]	ZnO	Ethylene glycol	No- surfactant	10-20	240	209
J. Michael Berg et al[15]	ZnO	Water	-	<50	30 (bath)	195
Ho Chang et al[16]	ZnO	DI Water	-	20	-	150

Berg et al. [15] investigated on the relationship between pH and zeta potential of 30 nm ZnO nanoparticles in ultrapure water. They reported isoelectric point (IEP) of ZnO (<50 nm in primary size) in the water is equal to 7.13 and average particle size when pH=7.13, pH=9, pH=9.5 and pH=11.05 equals 1173nm, 240nm, 226nm and 195 nm, respectively. However, Chang et al [16] reported IEP=9.27 for ZnO and minimum average size at pH=3 is equal to 150 nm. Table 1 is the summary of work related to preparation nanofluids with using sonication.

To measure stability of nanofluids scientists Derjaguin, Verwey, Landau and Overbeek developed a theory which is known as DLVO theory. They presented stability of a colloidal system depends on the total energy potential function (v_T). Total energy balance is mostly depends on components V_A (attractive contribution, Van der Waals attractive force) and V_R (repulsive contribution, electrical double layer repulsive forces).

$$v_A = \frac{-A}{(12\pi D^2)} \quad (2)$$

where A is the Hamaker constant (range 10^{-19} - 10^{-20} J) $A=1.9 \times 10^{-20}$ J (ZnO-water)[17] and D is the particle separation

$$V_R = 2 \pi \epsilon a \zeta^2 \exp(-\kappa D) \quad (3)$$

Where a is the particle radius, π is the solvent permeability, κ is a function of the ionic composition and ζ is the zeta potential.

Higher absolute value of zeta potential improves repulsive potential energy in a colloidal system. Figure 1 is the schematic of particle separation according to the DLVO theory[18].

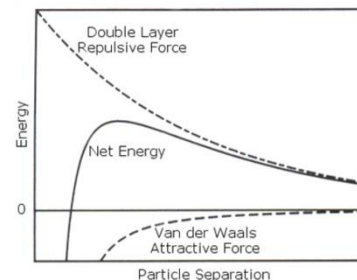


Figure 1 Variation of total potential energy for particle separation according to DLVO theory[18]

Nomenclature

R	[nm]	Nanoparticles radius
V_s	[m/s]	Sedimentation speed
A	[J]	Hamaker constant

Special characters

α	[KJ/ml]	Sonication energy density
ρ_s	[kg/m ³]	Density of solid nanoparticles
ρ_{BF}	[kg/m ³]	Density of based fluids
μ_{BF}	[Pa.s]	Viscosity of based fluids
ξ	[mV]	Zeta Potential
T	[K]	Absolute temperature
D	[m ² /s]	Diffusive constant
η_0	[Pa.s]	Dynamic Viscosity of the medium

EXPERIMENTAL PROCEDURE

Zinc Oxide nanoparticles were acquired from Nano structured and amorphous Material Inc, USA. ZnO nanoparticles with diameter of 20 nm, 99.5% of purity, 50m²/g Specific Surface Area (SSA), and true density of 5.606 g/cm³ were used. The size and morphology of ZnO nano-powder were examined with (A) Scanning Electron Microscopy (SEM) (B) Transmission Electron Microscopy (TEM) as shown in Figure 2 To perform measurement with SEM and TEM, the nanofluids samples first should be dried and then put them in the vacuum chamber. Therefore, some parts of the agglomeration of the nanoparticles will be as a result of laying different layers of the nanofluid over each other while drying. DI water has been supplied from Merck Company. Tetramethyl ammonium hydroxide pentahydrate (TAHP) (Aldrich company) with purity of more than 95% is used as a surfactant with ration of surfactant weight to nanoparticles weight, 5:100. Volume concentration of 0.05vol% ZnO nanofluids is prepared with using two-step method; with applying ultrasonic agitation probe. High accuracy scale (0.1 mg) is used to measure desired nanoparticles weight. First surfactant (THAP) (5% weight of ZnO nanoparticles) is dispersed in 40 ml DI water and stirring with magnetic stirrer for 10 min. Desired ZnO nanoparticles are dispersed in the based fluid. It is followed by putting the suspension which is in 80ml beaker in the constant bath at 13°C to remove excess heat from the suspension in order to prevent overheating of the sonicator probe. A sonicator (Qsonica Q-700 20KHz and 700 W with 3s pulse on 1s pulse off with amplitude (intensity) of 57%) is used to break down aggregation of particles. ZnO (concentration 0.05vol%) is dispersed with different sonication energy density ($\alpha = \frac{\text{Sonication energy input kJ}}{\text{Sample volume ml}}$)

range from $\alpha = 0$ [kJ/ml] to $\alpha = 10.8$ [KJ/ml] has been applied. Particle size distribution, average aggregation size and Zeta Potential of the colloidal solution were investigated by using Dynamic light scattering method with Zetasizer ZS (Malvern instrument limited, UK) versus sonication energy density. The equipment is using 4mW He-Ne 633 nm LASER as a source and it is capable to measure particle size range 0.3nm to 10000nm. The accuracy of the unit is better than +/-2% NIST traceable latex standards and repeatability +/- 1% of measured data for size and +/- 0.4% of measured data for the zeta

potential measurement. Measurement carries on at 25°C with assigning viscosity of water at 25°C to 0.8872 cP.

To measure mean hydrodynamic size stokes and Enstine [19] formula is used:

$$d = \frac{\kappa_B T}{3\pi D \eta_0} \quad (4)$$

where d is hydraulic diameter, κ_B Boltzman constant ($1.3806488 \times 10^{-23} \text{ m}^2 \text{ kg s}^{-2} \text{ K}^{-1}$), T absolute temperature, D diffusive coefficient and η_0 Dynamic viscosity of the medium.

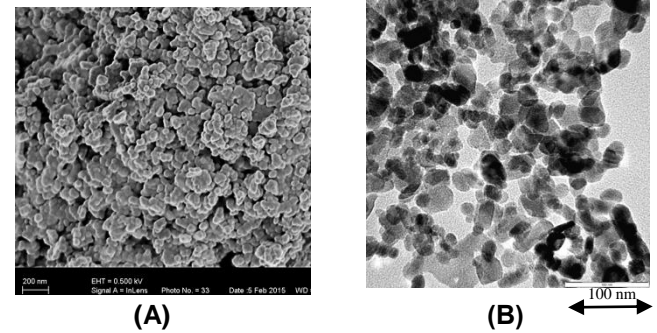
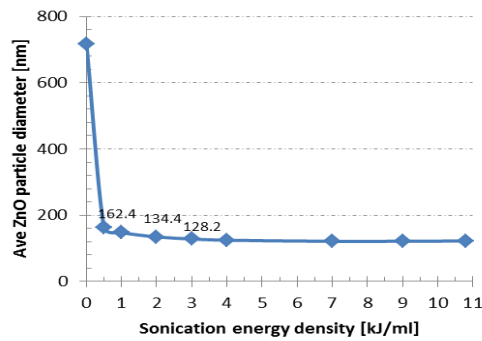


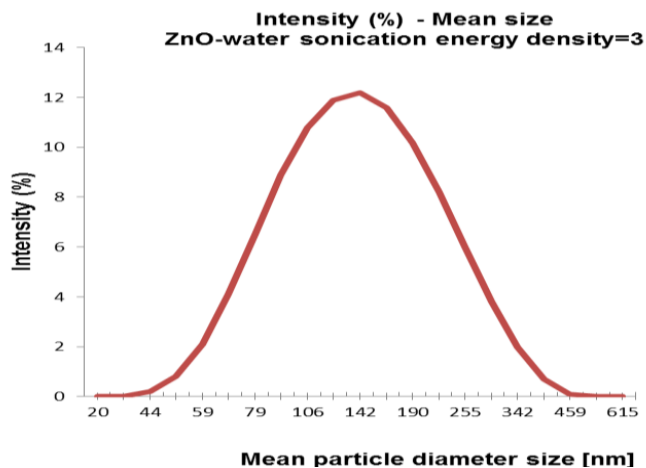
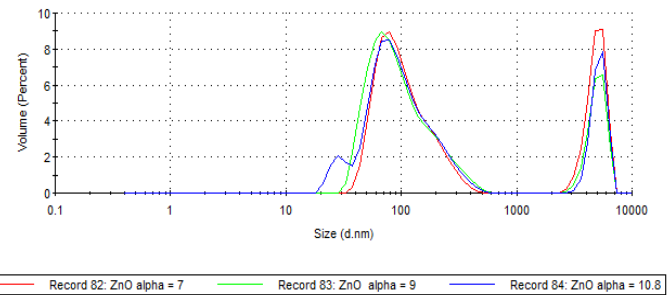
Figure 2 (A) SEM picture of dry nanoparticles of ZnO; (B) TEM picture of ZnO-water with surfactant

RESULTS AND DISCUSSION

In this research main focus is to find minimum possible average size in two step method preparation nanofluids with applying ultrasonication energy density. According to Stokes' law, reduction in average particle size reduce sedimentation rate and as a result in more stable nanofluids. Nano particles during production and storage process making aggregation with average size bigger than whatever manufactured specified. Figure 3 shows the average size of ZnO (by performing zetasizer measurement) in water suspension (nanofluid) with and without ultrasonications. It indicates that the average size of 718 nm when no ultrasonication made. Increasing energy density to 0.5 kJ/ml average size plunges from 718nm to 162 nm. Average size reduction become more linear after $\alpha = 1$ [kJ/ml] as results show sizes change from 147nm to 124 nm for $\alpha = 1$ and $\alpha = 4$, respectively. Further increase in sonication density couldn't break down average aggregation size furthermore. Figure 4. illustrates mean size distribution of ZnO for $\alpha = 3$ [kJ/ml] with range from 44nm to 396nm. Mean average size of 128nm, standard deviation (SD) of 69 nm and poly dispersity index (PDI) of 0.169 is reported. According to the Figure 5 further sonication result in big aggregation particles appear in the sample. However, many researchers with referencing to TEM or SEM microscopy photos using size of particles, which is close to a manufacturer claim, and applying that to predict thermophysical properties of nanofluids [20],[21] and [22], which could not be right.

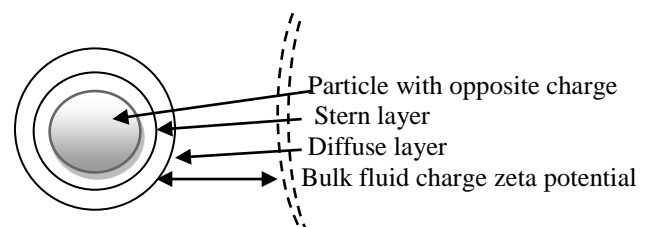
Average ZnO particle size-sonication energy density

Figure 3 Effect of sonication energy density on mean ZnO- water nanoparticle size

α (kJ/mL)	0	0.5	1	2	3	4	7	9	10.8
Ave-size (nm)	718	162	147	134	128	124	121	121	122
ZP [mv]	-33	-40	-40	-43	-44	-46	-48	-47	-46

Table 2. Sonication energy density and effect on mean size and zeta potential of 0.05 vol% ZnO- deionized water nanofluids (ZP, zeta potential)

Figure 4 Mean particles size of ZnO- water distribution for $\alpha=3$

Figure 5 Effect of high sonication energy density to aggregate big nanoparticles in ZnO-water nanofluids

In order to approach the stability of the samples, zeta potential of them needs to be measured. Zeta potential (ξ) is electrical potential between bulk fluids (medium) and charged acquired by liquid layer surrounding the particles surface which includes two parts, stern layer and diffuse layer (electrical double layer) which they showed in Figure 6 Zeta potential could give indication of stability of the colloidal dispersions. Higher absolute value of zeta potential indicates better stability of the suspensions. It is believed that suspensions with $\xi = \pm 30$ mV will be almost stable, $\xi = \pm 40$ to ± 60 mV gives good stability and $\xi \geq \pm 60$ indicates excellent stable of colloidal suspensions [23]. As a matter of fact, other factors, such as density difference of colloidal particle and based fluid also play an important role in stability of colloidal suspensions. Any efforts to improve absolute value of zeta potential could help to enhance stability of the colloidal systems, such as changing surface characteristics with adding surfactant and/or adjusting pH value far from the isoelectric point of a colloidal system.

Scaling up sonication energy density made an increase to absolute value of mean zeta potential from 33mV to 48 mV for $\alpha=0$ [kJ/ml] to $\alpha=7$ [kJ/ml], respectively. However, further sonication has got opposite effect on stability of the sample. Figure 7 shows zeta potential distribution for different sonication energy density. It is depicted from the Figure 8 that increasing sonication energy density increase distribution range of the zeta potential of the sample. Standard deviation for $\alpha=2$ [kJ/ml] and $\alpha=7$ [kJ/ml] changes from 6.5mV to 11 mV.


Figure 6 Schematic of zeta potential of a particle

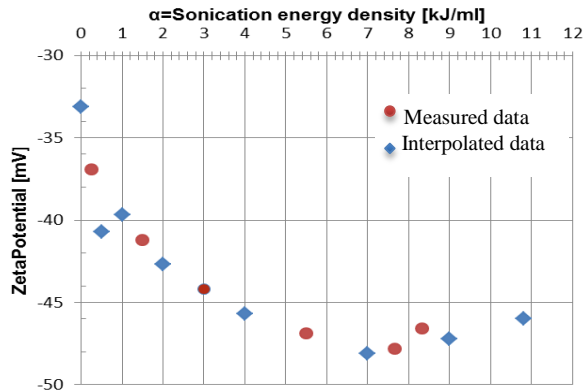


Figure 7 Effect of ultrasonication energy density on mean zeta potential of 0.05 vol% ZnO-water nanofluids

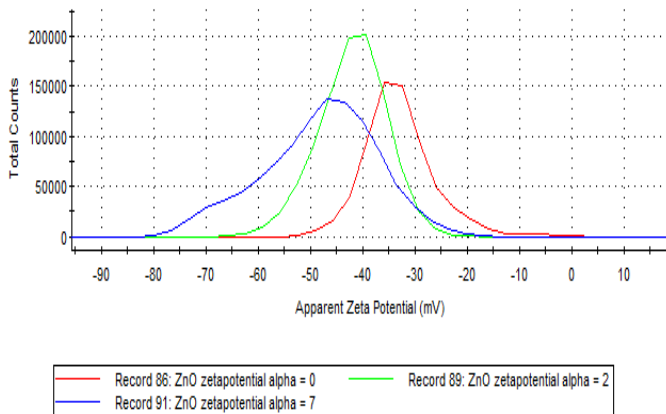


Figure 8 Influence of ultrasonication energy density on distribution of apparent zeta potential of ZnO-water nanofluids

Ultrasonication energy density could change mean size of the colloidal dispersion of ZnO-water nanofluids. It has found sonication energy density $\alpha = 3$ [kJ/mL] is adequate enough to give minimum mean size. However, with further sonication mean size just decrease 4nm, but big aggregated particles are detected in the sample, small tail as it seen in the particle distribution in Figure 5 These wide ranges of distribution ruin the stability of the sample and sedimentation is observed. Data reported from zeta potential also confirm that with increasing sonication, first zeta potential increase then with further increase in the sonication energy density zeta potential values decrease. Moreover, deviation of ultrasonication energy density from the optimum value ($\alpha=3$ kJ/ml) makes the distribution of zeta potential starch over the range that particles has got aggregation, thus it cause to accelerate sedimentation in the samples.

Size distribution of ZnO nanoparticles as well as high value for standard deviation of the samples pronounced that with using ultrasonication energy breaking down aggregation of the particles to primary size has not been achieved. Distribution

range of particles size makes also very difficult to produce stable ZnO monodispersed nanofluid.

Conclusion

Experimental mean aggregation size measurement of 0.05% volume fraction of Zinc Oxide-water nanofluids with zetasizer confirm effect of ultrasonication energy to reduce aggregation particle size, as well as, existence of optimum ultrasonication energy density to break down aggregation of specific nanoparticles in the based fluid to minimum possible aggregation size. It also has found further sonication causes very big aggregation of nanoparticles that could destroy stability of the prepared nanofluids.

Zeta potential measurements also confirmed the effect of sonication energy density on stability of colloidal suspension of ZnO-water nanofluids. Furthermore, resultant value for size distribution of ZnO-water (caused by aggregation) is much higher than primary size of nanoparticles which is claimed by manufacturers. Therefore, average size of nanofluids should be used in mathematical models to predict nanofluids thermophysical properties. The suggestion is to investigate more systematically by further experiments to conclude effect of sonication for different nanoparticles in different based fluids.

Acknowledgment:

The Authors duly acknowledge and appreciate the funding obtained from the following organizations: National Research Foundation of South Africa (NRF), CSIR and EIRT-seed.

References

- [1] S.U.S. Choi, Enhancing thermal Conductivity of Fluids with Nanoparticles, Proceedings of the 1995 ASME International Mechanical Engineering Congress and Exposition, USA, November 1995, Vol. 231, pp. 99-105
- [2] W. Yu, D.M. France, J.L. Routbort, S.U.S. Choi, Review and Comparison of Nanofluid Thermal Conductivity and Heat Transfer Enhancements, Heat Transfer Engineering, Vol. 29 No.5, 2008, pp. 432-460.
- [3] J. a. Eastman, S.U.S. Choi, S. Li, W. Yu, L.J. Thompson, Anomalously increased effective thermal conductivities of ethylene glycol-based nanofluids containing copper nanoparticles, Applied Physics Letters. Vol. 78, No. 6, 2001, pp. 718-720.
- [4] G. Colangelo, E. Favale, A. de Risi, D. Laforgia, Results of experimental investigations on the heat conductivity of nanofluids based on diathermic oil for high temperature applications, Applied Energy. Vol. 97, 2012, pp. 828-833.
- [5] H. Akoh, Y. Tsukasaki, S. Yatsuya, A. Tasaki, Magnetic properties of ferromagnetic ultrafine particles prepared by vacuum evaporation on running oil substrate, Journal of Crystal Growth. Vol. 45, 1978, pp. 495-500.

- [6] H. Bönemann, S.S. Botha, B. Bladergroen, V.M. Linkov, Monodisperse copper- And silver-nanocolloids suitable for heat-conductive fluids, *Applied Organometallic Chemistry*. Vol. 19, No. 6, 2005, pp. 768–773.
- [7] J. Boyle, I. Manas-Zloczower, D.L. Feke, Influence of particle morphology and flow conditions on the dispersion behavior of fumed silica in silicone polymers, *Particle and Particle Systems Characterization*. Vol. 21, No.3, 2004, pp. 205–212.
- [8] R. Wahab, Y.-S. Kim, H.-S. Shin, Synthesis, Characterization and Effect of pH Variation on Zinc Oxide Nanostructures, *Materials Transactions*. Vol. 50, No. 8, 2009, pp. 2092–2097.
- [9] G. Colangelo, E. Favale, A. de Risi, D. Laforgia, A new solution for reduced sedimentation flat panel solar thermal collector using nanofluids, *Applied Energy*. Vol. 111, 2013, pp. 80–93.
- [10] S.J. Chung, J.P. Leonard, I. Nettleship, J.K. Lee, Y. Soong, D. V. Martello, et al., Characterization of ZnO nanoparticle suspension in water: Effectiveness of ultrasonic dispersion, *Powder Technology*. Vol.194, No. 1-2, 2009, pp. 75–80.
- [11] K.S. Suganthi, K.S. Rajan, Temperature induced changes in ZnO–water nanofluid: Zeta potential, size distribution and viscosity profiles, *International Journal of Heat and Mass Transfer*. vol. 55, 2012, pp. 7969–7980.
- [12] K.S. Suganthi, V.L. Vinodhan, K.S. Rajan, Heat transfer performance and transport properties of ZnO – ethylene glycol and ZnO – ethylene glycol – water nanofluid coolants, *Applied Energy*. Vol. 135, 2014, pp. 548–559.
- [13] M. Kole, T.K. Dey, Effect of prolonged ultrasonication on the thermal conductivity of ZnO-ethylene glycol nanofluids, *Thermochimica Acta*. Vol. 535, 2012, pp. 58–65.
- [14] W. Yu, H. Xie, L. Chen, Y. Li, Investigation of thermal conductivity and viscosity of ethylene glycol based ZnO nanofluid, *Thermochimica Acta*. Vol. 491, 2009, pp. 92–96.
- [15] J.M. Berg, A. Romoser, N. Banerjee, R. Zebda, C.M. Sayes, The relationship between pH and zeta potential of ~ 30 nm metal oxide nanoparticle suspensions relevant to in vitro toxicological evaluations, *Nanotoxicology*. Vol. 3, No. 4, 2009, pp. 276–283.
- [16] H. Chang, M.H. Tsai, Synthesis and characterization of ZnO nanoparticles having prism shape by a novel gas condensation process, *Reviews on Advanced Materials Science*. Vol. 18, 2008, pp. 736–745.
- [17] Y. Zhang, Y. Chen, P. Westerhoff, K. Hristovski, J.C. Crittenden, Stability of commercial metal oxide nanoparticles in water, *Water Research*. Vol. 42, No. 8-9, 2008, pp. 2204–2212.
- [18] M. Instruments, Zeta potential: An Introduction in 30 minutes, *Zetasizer Nano Serles Technical Note*. MRK654-01. Vol. 1, 2011, pp. 8.
- [19] J.T. Edward, Molecular volumes and the Stokes-Einstein equation, *Journal of Chemical Education*. vol. 47, No.4, 1970, pp. 261-270.
- [20] J. Koo, C. Kleinstreuer, A new thermal conductivity model for nanofluids, *Journal of Nanoparticle Research*. Vol. 6, No. 6, 2004, pp. 577–588.
- [21] N. Masoumi, N. Sohrabi, a Behzadmehr, A new model for calculating the effective viscosity of nanofluids, *Journal of Physics D: Applied Physics*. vol. 42, No. 5, 2009, pp. 1-6.
- [22] C.H. Chon, K.D. Kihm, S.P. Lee, S.U.S. Choi, Empirical correlation finding the role of temperature and particle size for nanofluid (Al₂O₃) thermal conductivity enhancement, *Applied Physics Letters*. Vol. 87, No.15, 2005, pp. 1–3.
- [23] W. Yu, H. Xie, A review on nanofluids: Preparation, stability mechanisms, and applications, *Journal of Nanomaterials*. Vol. 2012, 2012, pp. 1-17

NANOFLUIDS; OPPORTUNITIES AND CHALLENGES

Sharifpur^{*1}, Meyer J.P.¹ and Hikmet Ş. Aybar²

¹Department of Mechanical and Aeronautical Engineering,
University of Pretoria, Pretoria, 0002, South Africa

²Department of Mechanical Engineering, Eastern Mediterranean University,
G. Magosa, KKTC, Mersin 10, Turkey

*Author for correspondence

E-mail: mohsen.sharifpur@up.ac.za

ABSTRACT

Nanofluids which are new heat transfer fluids have shown two important behaviors. First, their effective thermal conductivity can be much more than those of the conductivity of conventional heat transfer fluids. Secondly, magnetorheological nanofluids (MRNF) can control the viscosity when they are in a proper magnetic field. On the other hand, in general, nanofluids have shown more effective viscosity in comparison to the base fluids. The idea is to find the optimum range for each nanofluid to provide the maximum heat transfer performance. Consequently, they can significantly reduce the size and materials in the heat transfer applications. Therefore, investigation into the nanoparticles and nanofluid is important regarding material and energy management as well as environment issues. This study concerns on different issues and lack of research and information in nanofluids area to be involved in different industrial applications.

INTRODUCTION

Due to rapid technological developments, a lot of industrial equipment operate at a high temperature and/or speed for more power output. Therefore, cooling for sustaining desirable performance and durability of such devices and/or the rheological behavior of the lubricant or coolant fluid could be two of the technological issues encountered by high-tech industries. Conventional heat transfer fluids, generally have shown poor thermal conductivities in comparison with solids. Therefore, scattering solid particles into liquids could be a solution which is not a new idea, since it can be traced back to Maxwell's theoretical work in 1873 [1]. Consequently, fluids that contain mm- or μm - sized particles were used to increase the efficiency of thermal conductivity, but the particles were too large to pass through the channel smoothly. The other main problems were the rapid settling of the mm- or μm - sized particles in the base fluid and also the erosion by the particles was problematic. These days, modern technology makes it possible to produce smaller particle sizes than previous as nanoparticles which can be dispersed easily without rapid settling in the base fluid. Therefore, a novel generation of coolants called nanofluids was invented to meet the required cooling rate from heat transfer equipment [2].

This new and advanced heat transfer fluid can be described as the suspension of nanometer-sized (1-100nm) metallic, non-

metallic, polymeric particles, oxides and nanotubes in a conventional heat transfer fluid such as water, mineral oil, ethylene glycol, etc. It has the capability to be used in many industrial processes such as; power generation, chemical processes, heating and cooling processes, grinding process, fuel cells and micro-electronics. For example, their application in the automotive industry can minimize the size of radiators which in turn reduce the overall weight of the vehicle [3].

Nanofluids show better stability and rheological properties, higher thermal conductivity, and no penalty in pressure drop when compared with suspended particles of millimeter-or-micrometer dimensions. However, it looks the importance and opportunities of this new composite fluid as well as huge lack of research and information has not been noticed by researchers. They include:

- 1- Preparation of nanofluids and the stability issues
- 2- Prediction of thermal conductivity of nanofluids accurate for industrial condition
- 3- Prediction of viscosity of nanofluids for industrial condition
- 4- Nanofluids as heat transfer fluid
- 5- CFD simulation by using nanofluids
- 6- Health and safety issues

The purpose of this paper is to address the research potential, opportunities and the lack of research in the nanofluids area.

PREPARATION OF NANOFLUIDS AND THE STABILITY ISSUES

A nanofluid consists of nanoparticles blended into a base fluid. The particles have to be dispersed to form of a homogenous colloid.

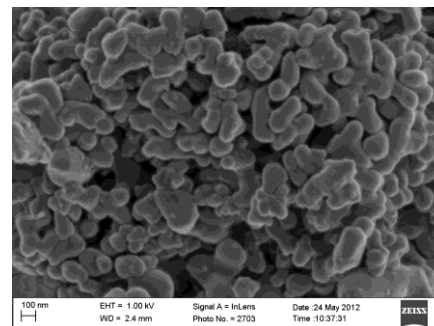


Figure 1 SEM image for Al_2O_3 nanoparticles with 80 nm size

There are two different methods to prepare nanofluids which consist of one step method and two-step method. In the one step method, usually the nanoparticles are produced chemically in the base fluid. However, in the two-step method, the nanoparticles are produced separately and then by using ultrasonic mixer [4] as well as other facilities like homogenizer, the nanoparticles will be suspended in the base fluids.

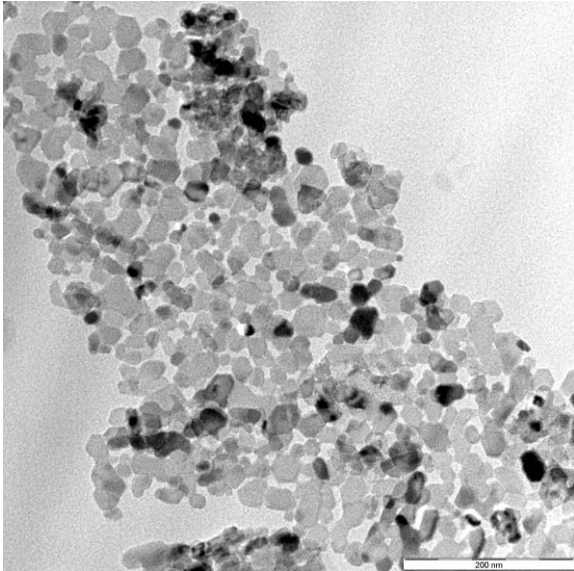


Figure 2 TEM image of MgO nanoparticles with 20 nm size

The one step method gives more stable nanofluids, but two-step method is more usual while there are not enough investigations into preparation of different nanofluids (different nanoparticles in different base fluids) for one step method.

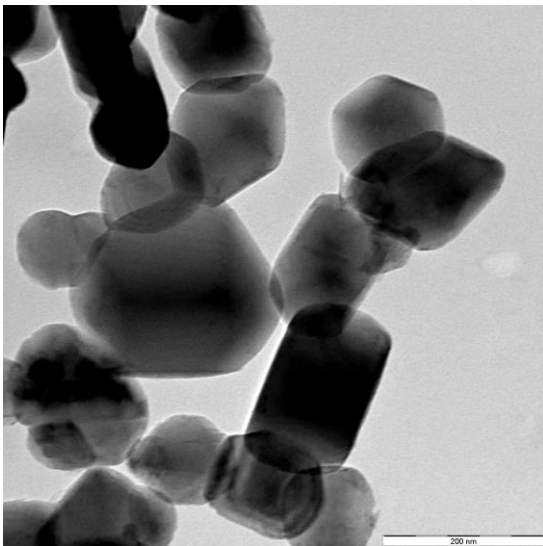


Figure 3 TEM image of MgO nanoparticles with 100 nm size

On the other hand, there is the lack of information for preparing a nanofluid by applying two-step method as well. Sentences like "it has been shown that the optimum preparation time when using ultrasound is 9 hours" [5] is not working for

nanofluids, while the number of hours is connected to the volume of the nanofluid up to an exact amount (concerning the energy per surface of the ultrasonicator) and then the sample must be divided in two or more. Furthermore, there is not an accurate equation to quantify the ultrasound energy (amplitude), frequency and the required time for different nanofluids. No reported information can be found for accurate expiry date of the stable nanofluids or nanoparticles in the market.

The other important issue is to find a way to show the degree of the stability of nanofluids. Most of the articles show the TEM or SEM or Zita-sizer analyses or X-ray diffraction peaks or tracking one of the measured parameters like thermal conductivity or viscosity by the time to show stability or no aggregation. However, none of them can show the stability of a nanofluid separately, but TEM or SEM and the others together. For example, Figure 1 shows an image of Al_2O_3 nanoparticles with 80 nm size [6] produced by a Scanning Electron Microscope (SEM) after several carbon coating as well as Figs. 2 and 3 show the TEM image for MgO nanoparticles 20 nm and 100 nm, respectively (SEM and all TEM images in this paper are taken at the University of Pretoria [7]). From the Figs. 1 to 3, it is possible to recognize the particle sizes, but they are not proper devices to find the aggregation while they need to dry the droplet of the nanofluids, this means in the Figs. 1 to 3 a lot of the particles can attach each other from different fluid layers in the process of drying. Therefore, it is not possible to recognize if the clustering happened in the nanofluid or it is as a result of drying process, or both.

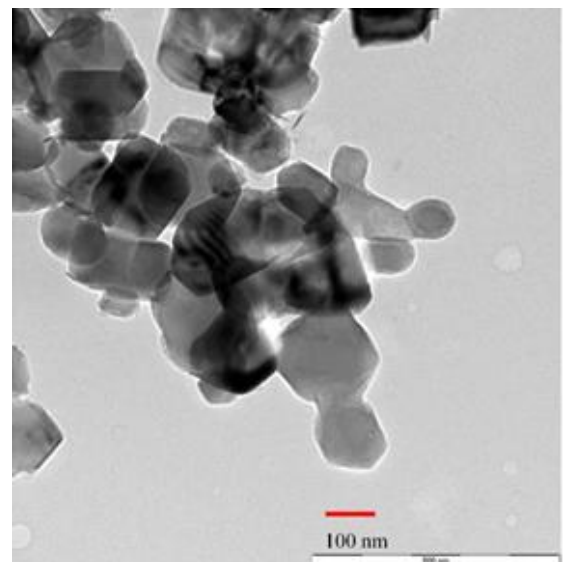


Figure 4 TEM image for MgO nanoparticles with 40 nm size (manufacturer claim)

In addition, all the researches working on nanofluids area need to use TEM or SEM to check if the particle size claimed by manufacturer is correct or not. For example Fig.4 shows TEM image for MgO nanoparticles with 40 nm size (manufacturer claim, Nanostructured Amorphous Inc., USA), which is clear that some of the particles are more than 100 nm.

THERMAL CONDUCTIVITY OF NANOFUIDS

Up to the present, the fundamental mechanism of enhanced thermal conductivity of nanofluids remains a key challenge in nanofluids research [8]. The conventional theoretical models cannot acceptably explain the enhancement of the thermal conductivity of nanofluids. It means, the increase in the thermal conductivity of nanofluids is not only because of the conduction, but also other mechanisms making a significant enhancement in thermal conductivity. For example; the specific surface area of the nanoparticles could be 1000 times larger than that of micro-particles, and because the heat transfer occurs on the surface of the particles, the high specific surface area of the nanoparticles increase the heat transfer conduction capability of nanofluids [9]. Therefore, it is important to understand the fundamental mechanism behind the heat transfer in nanofluids and also the important parameters which influence the heat transfer.

Nanofluids thermal conductivity enhancement consists of three major mechanisms: molecular-level layering of the liquid at the liquid/particle interface (nanolayer), Brownian motion of the nanoparticle and nanoparticle clustering. The following important parameters also affect the effective thermal conductivity of nanofluids: volume fraction of the nanoparticles, temperature, pH, dispersion, shape factor, nanolayer thickness, nanolayer thermal conductivity, the effect of settling down by time and the particle size effect on surface contact of liquid/particle interface. Up to present, more than 30 models have been developed in order to explain the thermal conductivity behaviour of nanofluids [8, 10]. However, most of them are based on experimental data (therefore, they are not valid for prediction out of the condition of the experiments) and there is not a model within them which can support the enhancement of effective thermal conductivity of nanofluids including all mechanisms and parameters.

VISCOSITY OF NANOFUIDS

Viscosity is an important consideration in the application of nanofluids as a lubricant or heat transfer fluids. Empirical investigations into the viscosity of nanofluids have shown that the existing theories, models and correlations have limitations. The parameters which have been applied so far in modeling nanofluid viscosity include volume fraction or concentration, temperature, packing fraction, thickness of the nanolayer, particle shape/aspect ratio, aggregate radius, inter-particle spacing and the capping layer [11, 12].

On the other hand the behavior of disperse magnetic nanofluids is of interest in the design of engineering systems requiring induced magnetic field effects for optimum performance. Therefore, the effective viscosity behavior of magneto-rheological nanofluids (MRNF) is principally governed by the presence of a magnetic field.

Although there are more than 30 empirical models available that predicts the effective viscosity of nanofluids, there is not a hybrid model that includes all influenced parameters.

HEAT TRANSFER APPLICATION OF THE NANOFUIDS

In the heat transfer application of nanofluids, the most important parameter is the interaction of the effective thermal conductivity (which increases by increasing the nanoparticles volume fraction) and the effective viscosity (which also increases by increasing the nanoparticles volume fraction). While they both increase, there must be an option volume fraction on different regime and cases (natural convection, laminar force convection and turbulence force convection) to enhance the heat transfer. On the other hand, nanofluids will find proper place in industries or designing different heat transfer systems if they can predict heat transfer accurately. In this way it requires a pair of thermal conductivity and viscosity for heat transfer calculations in each case. Now with more than 30 choices for each of them, it provides more than 1000 pair for the combination of thermal conductivities and viscosities which makes problem to find which the best is. Consequently, the idea is to find an accurate thermal conductivity and an accurate viscosity for each nanofluid while offering a model which can work for all nanofluids is not possible yet. Furthermore, the accurate correlations have also limitations concerning the condition of the experimental works.

CFD SIMULATION BY USING NANOFUIDS

Accurate CFD simulation is very important while it can easily bring nanofluids into industrial systems and designing different applicants. For CFD simulation there is still one main question, which asks if a nanofluid is a homogenous one phase mixture or a nanoparticle and a base fluid produce a two-component flow (or discrete phase flow) including slip velocity. If assuming a nanofluid as a homogenous one phase flow, therefore, it needs to introduce the properties of the nanofluid to the CFD software which again needs accurate correlation for thermal conductivity and viscosity. Consequently, considering the Discrete Phase Flow (DPF) looks better, but the mathematical modeling needs to be modified for nano-scale heat transfer while it does not work for all cases as the present modeling is [13].

RESEARCH OPPORTUNITIES IN NANOFUIDS

There are a lot of research opportunities and lack of information in this field. They include:

- Producing nanoparticles economically.
- Producing nanoparticles with a more accurate size.
- Investigation on environmentally friendly as well as health safe nanoparticles.
- Determining the thermal conductivity of nanofluids accurately.
- Estimation of the effective viscosity of nanofluids accurately.
- Research on energy density requirements for sonication.
- Image analyses of nanoparticles in the nanofluids
- Investigation on nanolayer thickness and properties

- Research on stabilizer (or surfactant) and how to make a nanofluid more stable as well as their expiry date
- Research on mathematical modelling of nanoscale heat transfer to use in the software packages, therefore, no needs to define different properties for nanofluids as discrete phase flow (not homogenous one phase mixture).

CONCLUSION

Nanofluids which are new heat transfer fluids show proper performance and opportunities for different applications. Unfortunately, there are lack of reported researches on comprehensive hybrid models for determining the properties of nanofluids, how to make stable nanofluids, finding health safe and environmental friendly nanoparticles, mathematical modelling which support the nano-scale heat transfer. Consequently, this important field requires the attention of researchers concerning the opportunities, challenges and the lack of information.

ACKNOWLEDGMENT

The Authors duly acknowledge and appreciate the funding obtained from the following organizations: National Research Foundation of South Africa (NRF), CSIR and EIRT-seed.

REFERENCES

- [1] Akbari, M., Behzadmehr, F. and Shahraki, F., Fully developed mixed convection in horizontal and inclined tubes with uniform heat flux using nanofluid, *International Journal of Heat and Fluid Flow* 29, pp. 545 – 556, 2008.
- [2] Saidur R., Leong K.Y. and. Mohammad H.A., A review on applications and challenges of nanofluids, *Renewable and Sustainable energy reviews* 15, pp. 1646-1668, 2011.
- [3] Kaka S. and Pramuanjaroenkij A., Review of convective heat transfer enhancement with nanofluids, *International Journal of Heat and Mass Transfer* 52, pp. 3187-3196, 2009.
- [4] Xuan Y., Li Q., Heat transfer enhancement of nanofluids, *International Journal of Heat and Fluid Flow* 21, pp. 58-64, 2000.
- [5] Kwak K. and Kim C., Viscosity and thermal conductivity of copper oxide nanofluid dispersed in ethylene glycol, *Korea-Australia Rheology Journal* 17-2, pp. 35-40, 2005.
- [6] *US Research Nanomaterials, Inc.*, <http://www.us-nano.com>.
- [7] *Laboratory for Microscopy and Microanalysis*, University of Pretoria, Pretoria, South Africa, 2012-2014.
- [8] Hikmet Ş. Aybar, Nwosu P.N., Sharifpur M., Azizian M.R., Mehrabi M. and Meyer J.P., *A Review of Thermal Conductivity Models of Nanofluids*, Heat Transfer Engineering, Vol. 36 (13) pp. 1085-1110, 2015.
- [9] Das, S.K., Choi, S.U.S., Yu, W. and Pradeep T., *Nanofluid science and technology*, John Wiley & Sons Inc., Hoboken, New Jersey, 2007.
- [10] Sharifpur M, Ntumba Tshimanga, Meyer JP, Parametric Analysis of Effective Thermal Conductivity Models for Nanofluids, *Proceedings of ASME 2012 International Mechanical Engineering Congress & Exposition*, IMECE2012-75305, 2012.
- [11] Josua P Meyer, Saheed A Adio, M Sharifpur and Paul N Nwosu, *The viscosity of nanofluids: a review of the theoretical, empirical and numerical models*, Heat Transfer Engineering, DOI:10.1080/01457632.2015.1057447, online: <http://www.tandfonline.com/doi/abs/10.1080/01457632.2015.1057447#abstract>
- [12] Meyer J.P., Nwosu P.N., Sharifpur M, Ntumba Tshimanga, Parametric Analysis of Effective Viscosity Models for Nanofluids, *Proceedings of ASME 2012 International Mechanical Engineering Congress & Exposition*, IMECE2012-93200, 2012,
- [13] Mandavi M., Sharifpur M, J.P. Meyer, CFD modelling of heat transfer and pressure drops for nanofluids through vertical tubes in laminar flow by DPM and Mixture model, *International Journal of Heat and Mass Transfer*, 88, 803-813, 2015

NUMERICAL SIMULATION OF THE DEPOSITION OF MAGNETIC BEADS ON THE WALLS OF MICROCHANNELS

Pallares J.
Department of Mechanical Engineering,
Universitat Rovira i Virgili,
Tarragona,
Spain,
E-mail: jordi.pallares@urv.cat

ABSTRACT

This paper analyzes numerical simulations of the trajectories of magnetic beads in a microchannel, with a nearby permanent cubical magnet, under different flow and magnetic conditions. The computed fractions of deposited particles on the walls are compared successfully with a new theoretically derived criterion that imposes a relation between the sizes of the magnet and the microchannel and the particle Stokes and Alfvén numbers to obtain the complete deposition of the flowing particles on the wall. In the cases in which all the particles, initially distributed uniformly across the section of the microchannel, are deposited on the walls, the simulations predict the accumulation of the major part of particles on the closest wall to the magnet and near the first half of the streamwise length of the magnet.

INTRODUCTION

The application of magnetism in fluidic microsystems has been used since the boom of microfluidics in the early 1900 with the concept of micro total analysis systems. Magnetic forces can be used to manipulate magnetic objects as magnetic particles or magnetically labelled cells. The movement of magnetic beads in microfluidic applications is usually controlled by permanent magnets or by magnetic fields generated by electric currents. Magnetohydrodynamic pumps, based on the generation of a magnetic field perpendicular to an electric field, can be used, as an alternative to pressure driven or electroosmotic flows, to produce flow in a conducting fluid. The same principle can be used for mixing. Plugs of ferrofluid can be moved with magnets to induce or to block the flow of an immiscible liquid. More information about these few examples and other applications involving magnetic forces in microflows can be found, for example, in the reviews of Gijs [1], Pamme [2] and Berthier and Silberzan [3] and the references therein.

Magnetic beads are constituted by nanoparticles of iron oxides embedded in a microsized biologically-compatible polymer (latex or polystyrene) sphere. The external surface of the sphere can be coated with biological molecules such as enzymes or DNA fragments which can be easily transported, by applying a magnetic field, towards specific locations or biological targets. Magnetic beads are used mostly for in vitro applications (biodiagnostics and biorecognition) and recently for in vivo applications, such as cancer treatment. In this case functionalized magnetic particles can be transported by the blood flow and retained by a magnet implemented in the treatment zone. For the most common applications the sizes of the magnetic particles range from 5 nm to 6 μm . The smallest

particles are used for applications in which the beads have to be dispersed by Brownian motion after the magnetic field is shut down while larger particles can be used to create large aggregates of particles. Magnetic beads used for biotechnology are usually paramagnetic because it is desired that the magnetic force vanish when the externally imposed magnetic field is switched off.

This study is focused in the prediction of the trajectories of magnetic beads in microchannels and the identification of the required magnetic and relevant physical properties needed for the deposition of the magnetic beads on the walls of the channel.

NOMENCLATURE

Al	[-]	Alfvén number, $Al = B^2/\mu_0\rho\bar{V}^2$
Al_p	[-]	Particle Alfvén number (see eq. 16)
B	[T]	Magnetic flux density
C_D	[-]	Drag coefficient
d	[m]	Diameter
F	[N]	Force
Fr	[-]	Densimetric Froude number $Fr = \bar{V}/(gh(1-\rho_f/\rho_p))^{1/2}$
g	[m s ⁻²]	Gravity acceleration
h	[m]	Height of the microchannel
L	[m]	Length
m	[kg]	Mass
M	[-]	Non-dimensional magnetic force
M_s	[A m ⁻¹]	Magnetization of the magnet
r	[m]	Position vector
Re	[-]	Reynolds number, $Re = \bar{V}h/\nu$
Re_p	[-]	Particle Reynolds number, $Re_p = \bar{V}_p - \bar{V} d_p/\nu$
St	[-]	Stokes number, $St = \rho_p d_p^2 \bar{V}/(18 \mu h)$
t	[s]	Time
u, v, w	[m s ⁻¹]	Velocity vector components
V	[m s ⁻¹]	Velocity
W	[m]	Width of the channel
x, y, z	[m]	Cartesian coordinates

Special characters

μ	[Pa s]	Dynamic viscosity
μ_0	[N A ⁻²]	Permeability of vacuum ($\mu_0 = 4\pi \cdot 10^{-7}$ N A ⁻²)
ν	[m ² s ⁻¹]	Kinematic viscosity
ρ	[kg m ⁻³]	Density
χ	[-]	Magnetic susceptibility

Subscripts

p	Particle
f	Fluid
m	Magnet, magnetic

Superscripts

*	Dimensionless quantity
---	------------------------

PHYSICAL AND MATHEMATICAL MODELS

The physical model is shown in Figure 1. A permanent cubical magnet is located above a straight microchannel with rectangular cross section. The distance between the top wall of the microchannel and the bottom of the magnet is L_{zm} . Two different positions of the magnet have been considered. A lateral position $L_{xm} = 0$ (see Fig. 1a) and a centered position for which the magnet is located symmetrically at the center of the microchannel (see Fig. 1b). Note that the lateral position generates a weaker magnetic field within the channel than the centered position but, in experiments, it allows the visual inspection of the region close to the magnet where magnetic beads are expected to deposit. In both cases the gravity vector acts along the negative z direction.

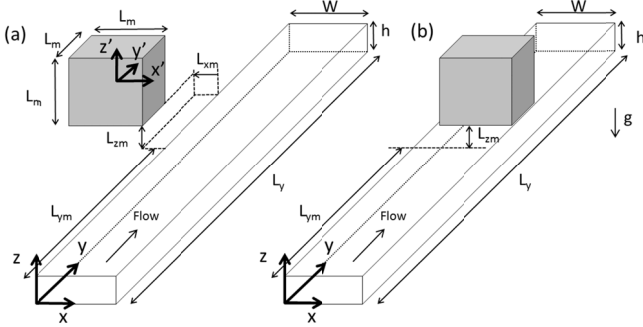


Figure 1 Physical model and coordinate systems

The flow is assumed to be incompressible, laminar, steady and the physical properties of the fluid constant. The particles are assumed to be spherical and they do not affect the flow according to the dilute approximation (i.e. one-way coupled Eulerian-Lagrangian approach). Under these hypotheses the flow can be described by the closed solution of the axial momentum equation for the pressure-driven fully developed flow. The axial velocity distribution, scaled with the averaged velocity, within the cross section of the microchannel is given by equation (1) (see for example Shah and London [4])

$$v^* = \frac{48}{\pi^3} \frac{\sum_{n=1,3,\dots}^{\infty} \frac{(-1)^{(n-1)/2}}{n^3} \left[1 - \frac{\cosh(n\pi(z-\frac{h}{2})/W)}{\cosh(n\pi h/2W)} \right] \cos(n\pi(x-\frac{W}{2})/W)}{\left[1 - \frac{192}{\pi^5} \left(\frac{W}{h}\right) \sum_{n=1,3,\dots}^{\infty} \frac{1}{n^5} \tanh(n\pi h/2W) \right]} \quad (1)$$

The particles are tracked with a Lagrangian approach based on the numerical solution of the kinematic equation and the force balance equation for each particle. The non-dimensional forms of these equations can be written as,

$$\frac{d\vec{r}_p^*}{dt^*} = \vec{V}_p^* \quad (2)$$

$$\frac{d\vec{V}_p^*}{dt^*} = \frac{1}{Fr^2} \frac{\vec{g}}{g} - \frac{3}{4} C_D \frac{\rho_f}{\rho_p} \frac{1}{d_p^*} |\vec{V}_p^* - \vec{V}^*| [\vec{V}_p^* - \vec{V}^*] + \frac{\chi \mu_0 M_s^2}{(4\pi)^2 \rho_p \bar{V}^2} (\vec{B}^* \cdot \vec{\nabla}^*) \vec{B}^* \quad (3)$$

The length and velocity scales used to obtain the non-dimensional variables are the height of the microchannel (h) and the average velocity of the flow (\bar{V}). The three terms on the right hand side of equation (3) are the gravity force, the drag force and the magnetic force. The lubrication force, the pressure gradient, as well as the near-wall lift have been neglected, as a first approximation. For micron-sized particles suspended in liquid laminar flows the Stokes number (St) and the particle Reynolds number (Re_p) are much lower than unity and the drag coefficient can be computed as, $C_D = 24/Re_p$. The form of the magnetic term in equation (3) is obtained from the dimensional form of the force per unit mass given in equation (4) [5], in which the initial magnetization of the particles is neglected [6].

$$\frac{\vec{F}_m}{m_p} = \frac{\chi}{\mu_0 \rho_p} (\vec{B} \cdot \vec{\nabla}) \vec{B} \quad (4)$$

The magnetic flux density has been computed using the analytical solution for permanent rectangular magnets reported by Furlani [7]. The components of the magnetic flux density are indicated in equations (5) to (7).

$$B_x^* = B_x \frac{4\pi}{\mu_0 M_s} = \sum_{k=1}^2 \sum_{n=1}^2 (-1)^{k+n} \log[F(x', y', z', x'_n, y'_1, y'_2, z'_k)] \quad (5)$$

$$B_y^* = B_y \frac{4\pi}{\mu_0 M_s} = \sum_{k=1}^2 \sum_{n=1}^2 (-1)^{k+n} \log[H(x', y', z', x'_1, x'_2, y'_n, z'_k)] \quad (6)$$

$$B_z^* = B_z \frac{4\pi}{\mu_0 M_s} = \sum_{k=1}^2 \sum_{n=1}^2 \sum_{l=1}^2 (-1)^{k+n+l} \tan^{-1}[G(x', y', z', x'_n, y'_l, z'_k)] \quad (7)$$

where F , H and G are defined as,

$$F(x', y', z', x'_n, y'_1, y'_2, z'_k) = \frac{(y' - y'_1) [(x' - x'_n)^2 + (y' - y'_1)^2 + (z' - z'_k)^2]^{1/2}}{(y' - y'_2) [(x' - x'_n)^2 + (y' - y'_2)^2 + (z' - z'_k)^2]^{1/2}} \quad (8)$$

$$H(x', y', z', x'_1, x'_2, y'_n, z'_k) = \frac{(x' - x'_1) [(x' - x'_1)^2 + (y' - y'_n)^2 + (z' - z'_k)^2]^{1/2}}{(x' - x'_2) [(x' - x'_2)^2 + (y' - y'_n)^2 + (z' - z'_k)^2]^{1/2}} \quad (9)$$

$$G(x', y', z', x'_n, y'_l, z'_k) = \frac{(x' - x'_n)(y' - y'_l)}{(z' - z'_k) [(x' - x'_n)^2 + (y' - y'_l)^2 + (z' - z'_k)^2]^{1/2}} \quad (10)$$

The system of reference, indicated with the prime symbol, used for equations (5) to (10) has its origin in the center of mass of the magnet (see Fig. 1) and (x'_1, y'_1, z'_1) and (x'_2, y'_2, z'_2) are

the coordinates of two diagonally opposed vertices of the magnet which has the magnetization aligned with the z' direction. For example, for a cubical magnet of size L_m , $x'_1 = y'_1 = z'_1 = -L_m/2$ and $x'_2 = y'_2 = z'_2 = L_m/2$.

Equations (2) and (3) were numerically integrated using the second order Crank-Nicolson scheme. The Lagrangian tracking code used here has been previously applied for the simulation of the turbulent dispersion of particles in forced [8] and natural convection [9] flows.

The fluid velocity at the position of the particle was computed using equation (1). In equation (3), the term $(\vec{B}^* \cdot \vec{\nabla}^*)\vec{B}^*$, at the particle position, has been computed analytically. The exact expressions for the three components were derived using *Mathematica* [10] and the output obtained with the `FortranForm` command was directly copied and pasted in the simulation code to avoid errors. A typical time step for the simulations was $\Delta t^* = 10^{-3}$.

The computational domain for the lateral position of the magnet had dimensions $L_x^* = 5, L_y^* = 100, L_z^* = 1$, while half of the microchannel was considered for the centered position because of symmetry with respect to the plane $x^* = 2.5$ (see Fig. 1.b). In this case the dimensions were $L_x^* = 2.5, L_y^* = 100, L_z^* = 1$. The computational domain was divided into $49 \times 499 \times 19$ equal volumes for the lateral case and into $99 \times 499 \times 19$ equal volumes for the centered case. A particle was placed at the center of each volume located at the inlet of the channel ($y^* = 0$) (i.e. $49 \times 19 = 931$ particles for the lateral case and $99 \times 19 = 1881$ particles for the centered case). The time marching scheme was initialized setting the velocity of the particle equal to that of the fluid at the specific location of the particle. The positions of the particles were stored and the instantaneous concentration of particles was determined by computing the number of particles in each volume.

This information was used to calculate the joint conditional probability for a particle to be at location x, y, z at time t , given that the particle was released at the position $x_0, y_0 = 0, z_0$ at time $t_0 = 0$. This probability can be used to extract information about the behavior of a continuous sources of particles located at the inlet of the channel. A similar approach is used in the simulation of scalar dispersion in turbulent flows at high Schmidt numbers [11]. This procedure based, on the Lagrangian tracking, overcomes the use of very fine grids, needed by the Eulerian approach, to capture the thin mixing interface of scalars (or clouds of particles) with very low molecular (or Brownian) diffusivity. For example, for 1 micron particles the Brownian diffusivity [3] at ambient temperature is $4 \cdot 10^{-13} \text{ m}^2/\text{s}$ and the corresponding Schmidt number is $2 \cdot 10^6$. Even for the 5 nm particles the Schmidt number is about 10^4 , which makes the numerical solution of the transport equation for the concentration of particles computationally very expensive using the conventional Eulerian approach.

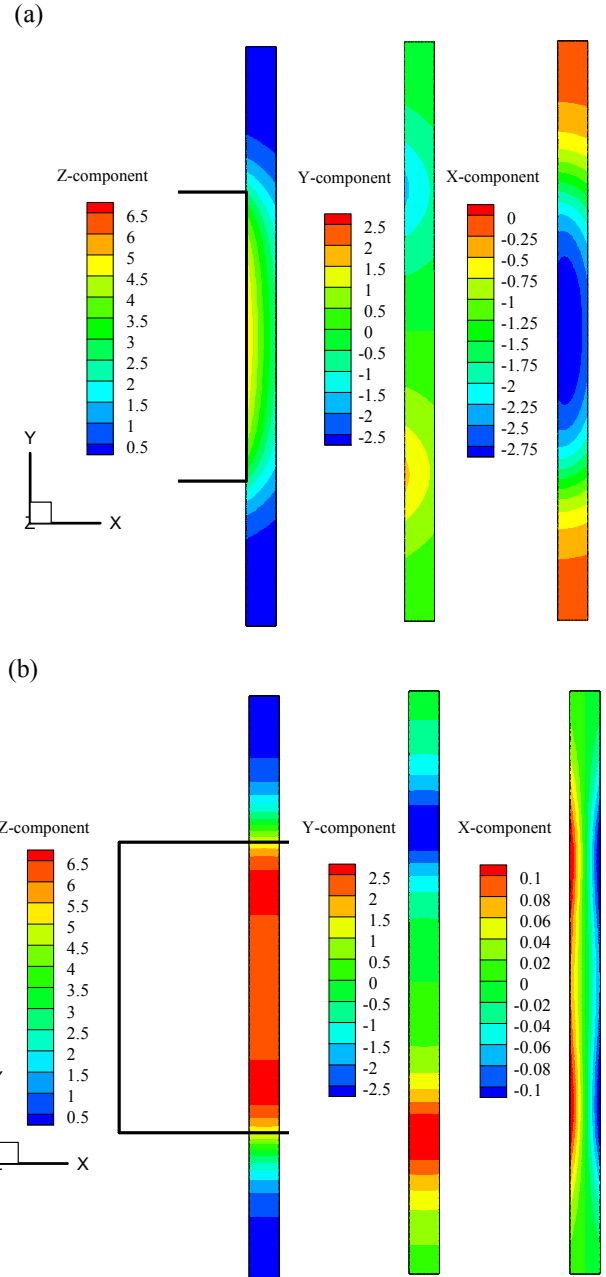


Figure 2 Contours of the three components of the magnetic gradient term, $(\vec{B}^* \cdot \vec{\nabla}^*)\vec{B}^*$ [mm^{-1}], (a) Lateral position (see Fig 1a). (b) Central position. The relative position of the magnet ($L_m=5 \text{ mm}$) with respect to the microchannel ($h=0.1 \text{ mm}$ $W=0.5 \text{ mm}$) is indicated by the black lines.

RESULTS AND DISCUSSION

As suggested by equation (3), the trajectories of the particles are dominated by the drag force, that is proportional to $(d_p^*)^{-2}$ and by the magnetic force, proportional to the group $M = \chi \mu_o M_s^2 / [(4\pi)^2 \rho_p \bar{V}^2]$ and to the non-dimensional term $(\vec{B}^* \cdot \vec{\nabla}^*)\vec{B}^*$. The first contribution to the magnetic force

depends on the magnetic characteristic of the particles (χ) and on the magnetization of the magnet. The second contribution depends only on the size of the magnet and its relative position with respect to the microchannel. As an example of the spatial distribution of the force generated by a magnet, Figure 2 shows the contours of the three components of the term $(\vec{B}^* \cdot \vec{\nabla})\vec{B}^*$ for the lateral (Fig. 2a) and centered (Fig. 2b) position of the magnet. The field corresponds to a cubical magnet ($L_m = 5 \text{ mm}$) located at $L_{zm} = 1 \text{ mm}$, above a microchannel ($h = 0.1 \text{ mm}$, $W = 0.5 \text{ mm}$). This distance is the typical width of the plastic cover of the microchips. The plots correspond to top views (x - y plane) of the microchannel. It can be seen that the lateral configuration (Fig. 2a) generates significant vertical (z) and lateral (x) forces towards the magnet. The centered case (Fig. 2b) generates intense vertical forces with maxima located close to the edges of the magnet and maximum axial (y) forces near the edges of the magnet.

To estimate the size and characteristics of the magnet needed to capture the magnetic beads which are flowing within a fluid we assume that the magnet is located at the top of the microchannel with a size larger or equal to the width of the microchannel.

The vertical velocity induced by the magnet can be estimated from the steady state vertical force balance on the particle. (see eq. 3)

$$\frac{dw^*}{dt^*} = -Fr r^{-2} - \frac{w^*}{St} + M(\vec{B}^* \cdot \vec{\nabla}^*)B_z^* = 0 \quad (11)$$

Rearranging equation (11), the dimensional vertical velocity can be written as,

$$w = \bar{V} St(-Fr r^{-2} + M(\vec{B}^* \cdot \vec{\nabla}^*)B_z^*) \quad (12)$$

The particles near the bottom wall of the channel need to travel vertically a distance h to reach the top wall of the channel, which is located below the magnet. If the vertical velocity is given by equation (12), then the time for the vertical travel is

$$t_z = \frac{h}{\bar{V}} \frac{1}{St(-Fr r^{-2} + M(\vec{B}^* \cdot \vec{\nabla}^*)B_z^*)} \quad (13)$$

To verify that all the particles are captured by the magnet we can consider that the particles located at the bottom wall of the channel should not travel along the streamwise direction a distance larger than the length of the magnet during the period of time given by equation (13). If we take the average flow velocity, as an upper limit, an estimation of the length of the magnet ($L_m = t_z \bar{V}$) can be written as,

$$L_m \approx \frac{h}{St(-Fr r^{-2} + M(\vec{B}^* \cdot \vec{\nabla}^*)B_z^*)} \quad (14)$$

The magnitude of the term $(\vec{B}^* \cdot \vec{\nabla}^*)B_z^*$ needs to be evaluated for the particular shape, size and location of the magnet. Figure 3 shows the magnitude of this term for different sizes of cubical magnets (L_m) located at the top of the microchannel of width W . The height of the microchannel is $h=100 \mu\text{m}$ and the bottom of the magnet is 1mm above the top wall of the microchannel. The value has been averaged in the volume of the microchannel below the magnet. It can be seen

that the average value of this term for the lateral configuration depends strongly on the aspect ratio of the microchannel while for the centered case this dependence is smaller.

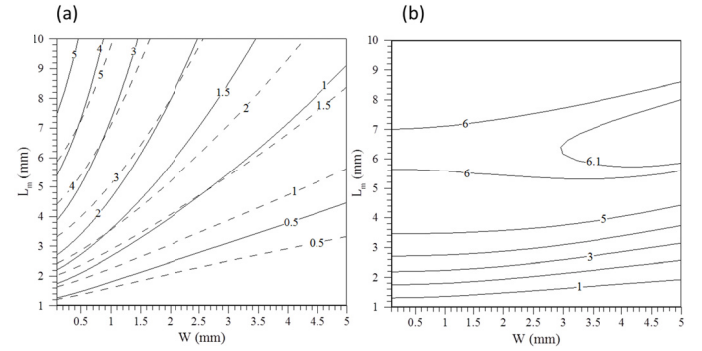


Figure 3 Volume averaged magnetic gradient term as a function of the channel width and the size of the cubical magnet for (a) the lateral position (see Fig. 1a) and (b) the centered position (see Fig 1b). The continuous contours correspond to the modulus of the vertical force $|(\vec{B}^* \cdot \vec{\nabla})B_z^*|$ [mm^{-1}] and the dashed line contours to the sum of the vertical and lateral force $\left[\left((\vec{B}^* \cdot \vec{\nabla})B_z^* \right)^2 + \left((\vec{B}^* \cdot \vec{\nabla})B_x^* \right)^2 \right]^{1/2}$ [mm^{-1}]

For cubical magnets with sizes between 4 mm and 10 mm the term is in the range $5000 \text{ m}^{-1} - 6000 \text{ m}^{-1}$. Additionally if we consider that the typical values of the magnetic saturation M_s for permanent magnets are between $5 \cdot 10^5 - 10^6 \text{ A/m}$ ($B_s=0.6 - 1.5 \text{ T}$) and that $0.1 \leq \chi \leq 1$ [6], $\rho_p \approx 1600 \text{ kg/m}^3$ and $h \approx 100 \mu\text{m}$ the contribution of the gravity force can be neglected in comparison with the magnetic force and equation (14) can be written as

$$\frac{L_m}{h} \approx \frac{1}{St (M(\vec{B}^* \cdot \vec{\nabla}^*)B_z^*)} \quad (15)$$

Equation (15) indicates that the non-dimensional size of the magnet needed to capture the particles depends on the particle Stokes number and on the term $M(\vec{B}^* \cdot \vec{\nabla}^*)B_z^*$ that represents the ratio between the applied magnetic energy and the particle inertia ($\rho_p \bar{V}^2$). This ratio is known in magnetohydrodynamics as the Alfvén number, $Al = B^2 / \mu_o \rho \bar{V}^2$ (see for example Lee and Choi [12]). Similarly we can introduce and define the particle Alfvén number as,

$$Al_p = \frac{\frac{\chi \mu_o M_s^2}{(4\pi)^2} \langle (\vec{B}^* \cdot \vec{\nabla}^*)B_z^* \rangle}{\rho_p \bar{V}^2} \quad (16)$$

In equation (16) $\langle (\vec{B}^* \cdot \vec{\nabla}^*)B_z^* \rangle$ is the non-dimensional volume averaged magnetic force. Equation (15) can be rewritten as,

$$\frac{L_m}{h} \approx \frac{1}{St Al_p} \quad (17)$$

Under physical conditions expressed above and at $Re = \bar{V}h/\nu = 1$, ($\bar{V} \approx 1 \text{ mm/s}$), the lengths predicted by equation (15) for $M_s=5 \cdot 10^5 \text{ A/m}$ and 10^6 A/m are 1.5 mm and 0.4 mm ,

respectively for $\chi = 1$, and 15 mm and 3.8 mm, for $\chi = 0.1$. This variability of the sizes, depending on the magnetic properties of the magnet (M_s) and of the particles (χ), suggests that the selection of the size of the magnet should be carried out with the knowledge of these properties.

Table 1 Physical parameters

d_p (m)	ρ_p (kg m ⁻³)	ρ_f (kg m ⁻³)	μ (Pa s)	L_m (m)	h (m)	W (m)	\bar{V} (m s ⁻¹)
10^{-6}	$1.6 \cdot 10^3$	10^3	10^{-3}	$5 \cdot 10^{-3}$	10^{-4}	$5 \cdot 10^{-4}$	0.1-0.01

Table 2 Non-dimensional parameters used in the simulations and predicted fraction of deposited particles

Case	Fr	M	Re	St	$Al_p^{(1)}$	L_m/h	$1/StAl_p$	% deposited
L1	3.68	$2.49 \cdot 10^4$	1	$8.89 \cdot 10^6$	$9.21 \cdot 10^3$	50	12	100
L2		$1.24 \cdot 10^4$			$4.60 \cdot 10^3$		24	100
L3	$3.68 \cdot 10^2$	$2.49 \cdot 10^2$	10	$8.89 \cdot 10^5$	$9.21 \cdot 10^1$		122	47
L4		$1.24 \cdot 10^2$			$4.60 \cdot 10^1$		244	33
C1	3.68	$2.49 \cdot 10^4$	1	$8.89 \cdot 10^6$	$1.47 \cdot 10^4$		8	100
C2		$1.24 \cdot 10^4$			$7.47 \cdot 10^3$		15	100
C3	$3.68 \cdot 10^2$	$2.49 \cdot 10^2$	10	$8.89 \cdot 10^5$	$1.47 \cdot 10^2$		77	71
C4		$1.24 \cdot 10^2$			$7.33 \cdot 10^1$		154	48

⁽¹⁾The volume averaged non-dimensional magnetic force, $\langle (\vec{B}^* \cdot \vec{\nabla}^*) B_z^* \rangle$, is 0.37 for the lateral cases and 0.59 for the centered cases ($L_m=5$ mm and $W=0.5$ mm) according to Figure 3

Numerical simulations of the trajectories of the particles have been carried out for the lateral position of the magnet (cases L1 to L4) and for central position (cases C1 to C4). The physical parameters and the conditions considered for the simulations are summarized in Tables 1 and 2. Table 2 shows that in cases L1, L2, C1 and C2, L_m/h is larger than $1/(StAl_p)$ and, in agreement with equation (17), all the particles initially released at the inlet of the microchannel are deposited on the walls. Figure 4 shows the fraction of deposited particles as a function of the parameter $1/(StAl_p)$. It can be seen that for $1/(StAl_p) < L_m/h = 50$ all the particles are deposited. For $1/(StAl_p) > 50$ a potential decrease of the fraction of deposited particles is observed. The potential fitting shown in Figure 4 predicts 90% of deposition at $1/(StAl_p) = 50$.

In Cases L3, L4, C3 and C4 only a fraction of the particles is captured by the magnet as indicated in Table 2. Figure 5 marks the initial positions of the particles that are not deposited on the walls and consequently they leave the computational domain through the outlet of the microchannel. It can be seen for the lateral cases L3 and L4 (Fig. 5.a) that the magnet deposits the particles initially located close to the top and to the right lateral walls. In Cases C3 and C4 (Fig. 5.b), in which the magnet is centered with respect to the microchannel, the captured particles are initially located close to the top and to both lateral walls because of the relatively low velocity of the flow near these lateral walls.

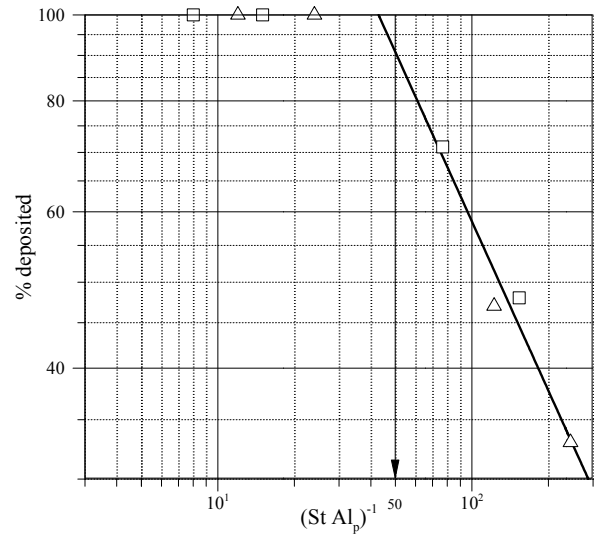
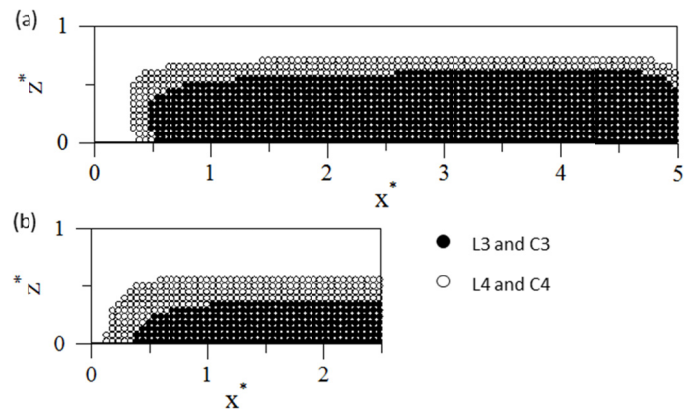

Figure 4 Fraction of particles deposited as a function of the parameter $1/(StAl_p)$. Triangles correspond to the lateral position of the magnet and squares to the centered position.

Figure 5 Initial positions of the particles that are not deposited on the walls of the microchannel. (a) Lateral position. (b) Central position (because of symmetry only half of the section is shown). Filled symbols correspond to cases L3 and C3 and open symbols to cases L4 and C4 (see Table 2)

Figure 6 shows the regions with high rates of particle deposition for cases L1 (Fig. 6.a-1 and 6.a-2) and C1 (Fig. 6.b-1 and 6.b-2) for which all the particles are deposited on the wall. The time is larger than 525 non-dimensional units which is large enough to allow the major part of the particles to reach their final location of deposition (i.e. one throughflow corresponds to 100 non-dimensional time units). To compute the deposition rate the computational domain has been divided into $49 \times 49 \times 19$ equal volumes for the lateral case and into $99 \times 49 \times 19$ equal volumes for the centered case. Note that initially a particle is located in the center of the volumes situated at the inlet of the computational domain. At each time step the number of new particles in each volume is stored and summed up during the simulation. Thus, this quantity represents the rate of increase of the number of particles in each

volume per time step, or equivalently, the rate at which the concentration of particles increases with respect to the concentration of particles at the inlet per time step. The isosurfaces plotted in Figs. 6.a and 6.b correspond to a value of 16 and 6, respectively. In the case of the lateral position of the magnet (Figs. 6.a) the particles are deposited near the lateral wall closest to the magnet, while for the centered position (Figs. 6.b) the particles are deposited on the top wall. In both cases the simulations predict the location of the accumulations below leading edge of the magnet near the first half of the streamwise length of the magnet.

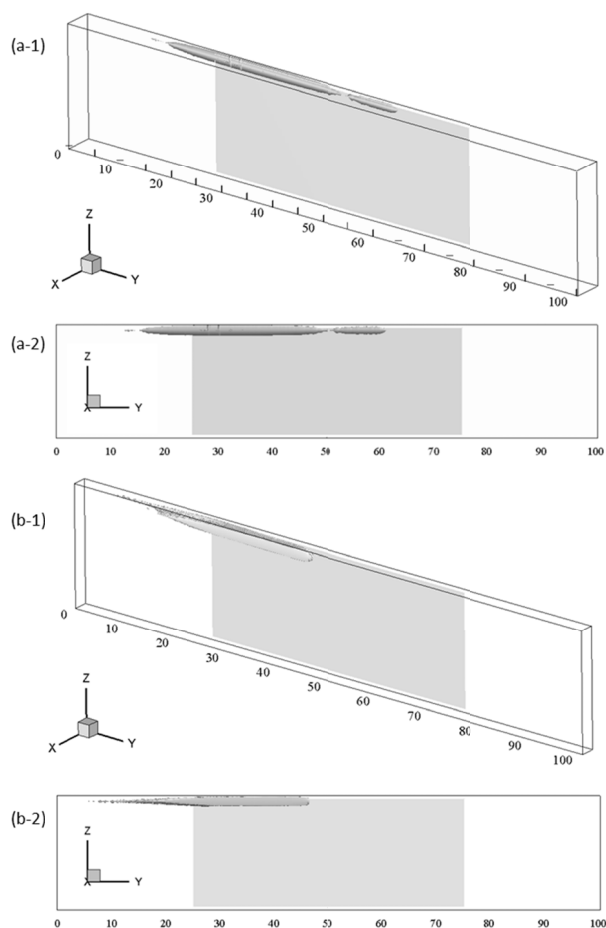


Figure 6 Isosurfaces of particle concentrations. (a) Case L1. (b) Case C1 (see Table 2). The vertical scale of the channel has been enlarged for better visualization and the projection of the magnet located between $25 < x < 75$ is shown in grey.

CONCLUSIONS

In this study we analyzed numerical simulations of the trajectories of magnetic beads in a straight microchannel under the influence of a nearby permanent cubical magnet for different flow and magnetic conditions. Analytically derived local fluid velocities and local magnetic forces have been used to track the particles. A centered position and a lateral position of the magnet above the microchannel are considered. It has been found theoretically that the fraction of the particles

deposited on the walls of the microchannel depends on the Stokes and Alfvén particle numbers and that the size of the magnet should be larger than the height of the microchannel divided by the Stokes and Alfvén particle numbers to capture all the particles uniformly distributed across the section of the microchannel. The results of the numerical simulations are in agreement with this criterion. The Lagrangian tracking of the particles has shown that accumulations of deposited particles occur on the top wall of the microchannel for the centered position of the magnet, while for the lateral position the accumulation is located on the lateral wall closest to the magnet. In both cases the simulations predict the location of the accumulations below leading edge of the magnet near the first half of the length of the magnet.

Acknowledgements

This study has been supported by the Spanish Ministerio de Economía y Competitividad under project CTQ2013-46799-C2-1-P

REFERENCES

- [1] Gijs M.A.M. Magnetic bead handling on-chip: new opportunities for analytical applications *Microfluidics and Nanofluidics*, Vol. 1, 2004, pp. 22–40
- [2] Pamme N. Magnetism and microfluidics, *Lab on a Chip*, Vol. 6, 2006, pp. 24–38
- [3] Berthier J., and Silberzan P. *Microfluidics for biotechnology*, 2009, Artech House, Boston
- [4] Shah R.K., and London A.L., *Laminar flow forced convection in ducts*, 1978, Academic Press, New York
- [5] Verbruggen B., Tóth T., Cornaglia M., Puers R., Gijs M.A., and Lammertyn, J. Separation of magnetic microparticles in segmented flow using asymmetric splitting regimes, *Microfluidics and Nanofluidics*, Vol. 18, 2014, pp. 91-102
- [6] Shevkoplyas S.S., Siegel A.C., Westervelt R.M., Prentiss M.G., and Whitesides G.M. The force acting on a superparamagnetic bead due to an applied magnetic field, *Lab on a Chip*, Vol. 7, 2007, pp. 1294-1302
- [7] Furlani E.P., *Permanent magnet and electromechanical devices. Materials, analysis and applications*, 2001, Academic Press, San Diego
- [8] Pallares J., Vernet A., and Grau F.X., Effect of the instantaneous turbulent flow structures on the particle distribution near the wall of a channel, *European Journal of Mechanics B/Fluids*, Vol. 46, 2014, pp. 144-153
- [9] Pallares J., and Grau F. X. Particle dispersion in a turbulent natural convection channel flow, *Journal of Aerosol Science*, Vol. 43, 2012, pp. 45-56
- [10] *Mathematica*. Wolfram Research. Champaign, IL. USA
- [11] Papavassiliou D.V., and Hanratty T.J., Transport of a passive scalar in a turbulent channel flow, *International Journal of Heat and Mass Transfer*, Vol. 40, 1997, pp. 1303–1311
- [12] Lee D., and Choi H. Magnetohydrodynamic turbulent flow in a channel at low magnetic Reynolds number, *Journal of Fluid Mechanics*, Vol. 439, 2001, pp. 367-394

NEW TYPE OF INSTABILITY NEAR CHARGED SELECTIVE SURFACE CAUSED BY THE JOULE HEATING

Ganchenko G.S.,¹ Khasmatulina N.Yu.,² Demekhin E.A.,³ and Amiroudine S.⁴

¹*Department of Computational Mathematics and Computer Science,
Kuban State University, Krasnodar, 350040, Russian Federation.*

²*Department of Mathematical Modelling, Kuban State University, Krasnodar, 350040, Russian Federation.*

³*Laboratory of Electro-Hydrodynamics of Micro- and Nanoscales,
Department of Mathematics and Computer Science,
Financial University, Krasnodar, 350051, Russian Federation.*

⁴*Université Bordeaux, I2M, UMR CNRS 5295, 16 Av. Pey-Berland, 33607 Pessac, France*

ABSTRACT

An intense development of nano- and biotechnologies in the past two decades has resulted in the appearance of a number of new problems of electrohydrodynamics and in revising the importance of certain problems having a long history. The study of the space charge in the electric double layer near charge-selective surfaces (permselective membranes, electrodes, or systems of micro- and nanochannels) is a fundamental problem of modern physics first addressed by Helmholtz. In the case of a small size system (fraction of mm), the electro-osmotic effects and the concentration-polarization phenomena result in a special kind of instability, the electrokinetic instability, which causes electro-osmotic flow and micro-vortex formation. The electrokinetic instability was discovered theoretically by the Rubinstein and Zaltzman in 2000 and was confirmed experimentally in 2007–2008. In the present work the influence of the Joule heating on the electrokinetic instability is investigated theoretically. The problem is described by the strongly nonlinear coupled Nernst–Planck–Poisson–Stokes system along with the energy transfer equation. A simple analytical solution for the marginal stability curves based on the Rubinstein–Zaltzman approach is found. The physical mechanism of the thermal instability is found to be very different from the well-known Rayleigh–Bénard convection: the Joule heating can either destabilize or stabilize the steady state depending on the space charge region location with respect to the gravity vector. For the destabilizing case the short wave Rubinstein–Zaltzman instability is replaced by the long wave thermal instability. The study is complemented by numerical investigations both of linear and nonlinear instabilities near a charged selective surface. Galerkin pseudo-spectral method is applied. There is a good qualitative agreement with the analytics. Possible explanation of discrepancy between experimental data and our previous theoretical Volt-Current characteristics is highlighted.

INTRODUCTION

Problems of electrokinetics have recently attracted a great deal of attention due to rapid developments in

micro-, nano-, and bio-technology. Among the numerous modern applications of electrokinetics are micro-pumps, desalination devices, biological cells, electro-polishing of mono- and poly-crystalline aluminium, and the growth of aluminium oxide layers for creating micro- and nano-scale regular structures such as quantum dots and wires.

There is also a fundamental interest in the problem. The study of the space charge in an electric double-ion layer in an electrolyte solution between semi-selective ion-exchange membranes under a potential drop is a fundamental problem of modern physics, first addressed by Helmholtz. Rubinstein and Shtilman [1] completely described the regime of limiting currents (see also [2–4]). Hydrodynamics was not involved in either of the under-limiting or limiting regimes, and both regimes were one-dimensional.

It was first theoretically predicted by Rubinstein and Zaltzman [5], [6] that the transition from limiting to overlimiting currents is connected with a novel type of electro-hydrodynamic instability, which is known as electrokinetic instability. This instability triggers a hydrodynamic flow and, in turn, intensifies the ion flux which is responsible for the overlimiting currents. The first direct experimental proof of the electroconvective instability that arises with an increasing potential drop between ion-selective membranes was reported by Rubinstein *et al.* [7], who managed to show the existence of small vortices near the membrane surface. A unified theoretical description of the linear electrokinetic instability, valid for all three regimes, was presented by Zaltzman and Rubinstein [8], based on a systematic asymptotic analysis of the problem.

The DNS for two-dimensional (2D) Nernst–Planck–Poisson–Stokes (NPPS) equations were considered in [9–14]. A full scale direct numerical simulation (DNS) for the three-dimensional (3D) formulation is presented in Demekhin *et al.* [15].

In all the aforementioned theoretical and numerical analyses, thermal effects are neglected. On the other hand, one of the major technological concerns in electrokinetically actuated microflows is the Joule heating [16–21]. Moreover, Zabolotsky and Nikonenko [22] found experimentally that a typical temperature difference between the electrolyte inside the membrane system and the environment can be as much as several degrees. Such

a temperature difference can not only have an influence on the electrokinetic instability near a charge-selective surface, but can also be a driving force for a new kind of instability based on the spatial nonuniformity of the electrical conductivity. It can also be shown that Joule heating has a significant effect on the voltage-current (VC) characteristic. These phenomena are investigated in the present paper.

STATEMENT

A symmetric, binary electrolyte with a diffusivity of cations and anions \tilde{D} , dynamic viscosity $\tilde{\mu}$, and electric permittivity $\tilde{\varepsilon}$, and bounded by ideal, semiselective ion-exchange membrane surfaces at $\tilde{y} = 0$ and $\tilde{y} = \tilde{h}$ with a potential difference $\Delta\tilde{V}$ between these surfaces, is treated, see Fig. 1. The Joule heating generated by the passage of a current through the electrolyte is taken into account. Notations with tilde are used for the dimensional variables, as opposed to their dimensionless counterparts without a tilde. $\{\tilde{x}, \tilde{y}\}$ are the coordinates, where \tilde{x} is directed along the membrane surface and \tilde{y} is normal to it.

The electroconvection is described by the following equations,

- ion transport for the concentration of cations and anions \tilde{c}^\pm ,

$$\frac{\partial \tilde{c}^\pm}{\partial \tilde{t}} + \tilde{\mathbf{u}} \cdot \nabla \tilde{c}^\pm = \tilde{D} \left(\pm \nabla \cdot \left(\frac{\tilde{F}}{\tilde{R}\tilde{T}} \tilde{c}^\pm \nabla \tilde{\Phi} \right) + \nabla^2 \tilde{c}^\pm \right), \quad (1)$$

- Poisson equation for the electric potential $\tilde{\Phi}$,

$$\nabla^2 \tilde{\Phi} = \frac{\tilde{F}(\tilde{c}^- - \tilde{c}^+)}{\tilde{\varepsilon}}, \quad (2)$$

- Stokes equations for a creeping flow,

$$\nabla \tilde{\Pi} = \tilde{\mu} \nabla^2 \tilde{\mathbf{u}} + \tilde{F} \nabla \tilde{\Phi} (\tilde{c}^- - \tilde{c}^+) + \tilde{g} \tilde{r}_0 \tilde{\beta} (\tilde{T} - \tilde{T}_0) \mathbf{e}_y, \quad (3)$$

$$\nabla \cdot \tilde{\mathbf{u}} = 0,$$

- Energy equation,

$$\frac{\partial \tilde{T}}{\partial \tilde{t}} + \tilde{\mathbf{u}} \cdot \nabla \tilde{T} = \tilde{a} \nabla^2 \tilde{T} - \frac{\tilde{\mathbf{I}} \cdot \nabla \tilde{\Phi}}{\tilde{c}_p \tilde{r}_0}, \quad (4)$$

where \tilde{F} is Faradays constant, \tilde{R} is the universal gas constant, \tilde{T}_0 is the temperature of the environment, $\tilde{\varepsilon}$ is the electric permittivity, \tilde{g} is the acceleration due to gravity, \tilde{r}_0 is the density, $\tilde{\beta}$ is the thermal expansion coefficient,

\tilde{c}_p is the specific heat capacity, and \tilde{a} is the thermal diffusivity. In the above equations, the two-dimensional case is treated; $\tilde{\mathbf{u}} = (\tilde{U}, \tilde{V})$ is the fluid velocity vector; $\tilde{\Pi}$ is the pressure. Equation (3) contains the term of buoyancy force in the Boussinesq approximation, where the unit vector \mathbf{e}_y is directed along the y -axis. The energy equation contains the source term associated with the Joule heating of the electrolyte.

$$\tilde{\mathbf{I}} = -\frac{\tilde{F}^2 \tilde{D}}{\tilde{R}\tilde{T}} (\tilde{c}^+ + \tilde{c}^-) \nabla \tilde{\Phi} - \tilde{F} \tilde{D} \nabla (\tilde{c}^+ - \tilde{c}^-), \quad (5)$$

has to be taken for the source term in (4). This system of dimensional equations is complemented by the following boundary conditions (BC),

$$\tilde{y} = 0: \quad \tilde{c}^+ = \tilde{p}, \quad -\frac{\tilde{F} \tilde{c}^-}{\tilde{R}\tilde{T}} \frac{\partial \tilde{\Phi}}{\partial \tilde{y}} + \frac{\partial \tilde{c}^-}{\partial \tilde{y}} = 0,$$

$$\tilde{\Phi} = 0, \quad \tilde{\mathbf{u}} = \mathbf{0}, \quad -\frac{\partial \tilde{T}}{\partial \tilde{y}} + \frac{\tilde{\alpha}}{\tilde{\lambda}_T} (\tilde{T} - \tilde{T}_0) = 0, \quad (6)$$

$$\tilde{y} = \tilde{h}: \quad \tilde{c}^+ = \tilde{p}, \quad \frac{\tilde{F} \tilde{c}^-}{\tilde{R}\tilde{T}} \frac{\partial \tilde{\Phi}}{\partial \tilde{y}} - \frac{\partial \tilde{c}^-}{\partial \tilde{y}} = 0,$$

$$\tilde{\Phi} = \Delta\tilde{V}, \quad \tilde{\mathbf{u}} = \mathbf{0}, \quad \frac{\partial \tilde{T}}{\partial \tilde{y}} + \frac{\tilde{\alpha}}{\tilde{\lambda}_T} (\tilde{T} - \tilde{T}_0) = 0, \quad (7)$$

where $\tilde{\alpha}$ is the heat transfer coefficient and $\tilde{\lambda}_T$ is the thermal conductivity of the fluid. The first boundary condition, prescribing an interface concentration equal to that of the fixed charges inside the membrane, is asymptotically valid for large \tilde{p} and was first introduced by Rubinstein (see, for example, Ref. [8]). This condition prevents the calculation of the complete solution within the membrane. The second boundary condition means no total flux for negative ions, the third condition is a fixed potential drop, the fourth condition is that the velocity vanishes at the rigid surface, and the last condition corresponds to the mixed thermal boundary conditions. The spatial domain is assumed to be infinitely large in the \tilde{x} -direction, and the boundedness of the solution as $\tilde{x} \rightarrow \pm\infty$ is imposed as a boundary condition. Such a statement, but without thermal effects, is presented in [8].

In order to make the system dimensionless, the characteristic quantities are as follows: \tilde{h} — the characteristic length, the distance between the membranes; \tilde{h}^2/\tilde{D} — the characteristic time; $\tilde{\mu}$ — the dynamic viscosity; \tilde{c}_∞ — the typical electrolyte concentration (e.g., the average concentration in the system); the thermic potential $\tilde{\Phi}_0 = \tilde{R}\tilde{T}_0/\tilde{F}$ is taken as the characteristic potential with $\tilde{T}_0 = 300 \text{ K}$. The characteristic temperature can be obtained from the balance between the Joule heating and the energy loss to the environment,

$$\tilde{T}_{ch} = \frac{\tilde{\Phi}_0 \tilde{D} \tilde{F} \tilde{c}_\infty}{\tilde{a} \tilde{c}_p \tilde{r}_0} \frac{\tilde{\lambda}_T}{\tilde{\alpha} \tilde{h}}.$$

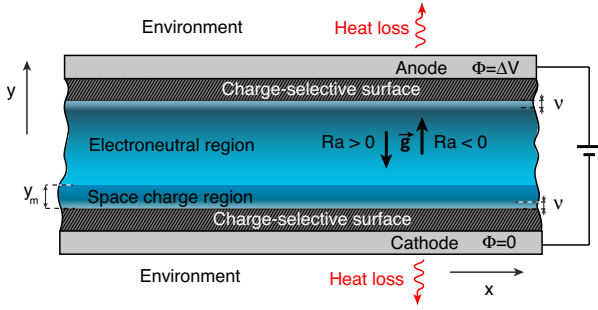


FIG. 1. Schematics of the system. Space charge region near $y = 0$, $0 < y < y_m$, includes thin electric double layer (EDL), which exists also near $y = 1$. The acceleration vector \mathbf{g} can be either co-directed ($Ra < 0$) or counter-directed ($Ra > 0$) to the y -axis.

Small deviations of the electrolyte temperature from the environmental temperature are considered. The dimensionless characteristic electric current j at the membrane surface is

$$j = c^+ \frac{\partial \Phi}{\partial y} + \frac{\partial c^+}{\partial y}, \quad \text{for } y = 0. \quad (8)$$

In our case, the channel surface is permeable only by the cations, and, hence, j is determined only by the flux of the positive ions.

The problem is described by eight dimensionless parameters: ν is the dimensionless Debye length or Debye number, \varkappa is a coupling coefficient between the hydrodynamics and the electrostatics (it is essential that the coupling coefficient depends only upon the physical properties of the electrolyte), ΔV is the potential drop between the membranes, Ra is the Rayleigh number, Bi is the Biot number (characterizing the system's thermal insulation with respect to the environment), Le is the Lewis number, p is the membrane interface concentration in the boundary conditions (6) and (7):

$$\begin{aligned} \nu &= \frac{\tilde{\lambda}_D}{\tilde{h}}, \quad \varkappa = \frac{\tilde{\varepsilon} \tilde{\Phi}_0^2}{\tilde{\mu} \tilde{D}}, \quad \Delta V = \frac{\tilde{\Delta V}}{\tilde{\Phi}_0}, \\ Ra &= \frac{\tilde{F} \tilde{g} \tilde{\beta} \tilde{\Phi}_0 \tilde{c}_\infty \tilde{h}^2}{\tilde{a} \tilde{c}_p \tilde{\mu} \tilde{\alpha}}, \\ Bi &= \frac{\tilde{\alpha} \tilde{h}}{\tilde{\lambda}_T}, \quad Le = \frac{\tilde{D}}{\tilde{a}}, \quad p = \frac{\tilde{p}}{\tilde{c}_\infty}, \end{aligned} \quad (9)$$

where $\tilde{\lambda}_D = \sqrt{\frac{\tilde{\varepsilon} \tilde{\Phi}_0}{\tilde{F} \tilde{c}_\infty}}$ is the Debye length. In order to give an idea of the values of the above dimensionless numbers, typical dimensional values for an aquatic solution of $NaCl$ for normal conditions are taken to be $\tilde{\Phi}_0 = 0.025 V$, $\tilde{D} = 2 \times 10^{-9} m^2/s$, $\tilde{\varepsilon} = 7 \times 10^{-10} (C^2 s^2)/(kg m^3)$, $\tilde{r}_0 = 10^3 kg/m^3$, $\tilde{\beta} = 2.07 \times 10^{-4} K^{-1}$, $\tilde{c}_p = 4182 J/(kg K)$, $\tilde{a} = 1.53 \times 10^{-7} m^2/s$, $\tilde{\lambda}_T = 0.602 W/(mK)$. Channel width varies in the

range of micro- to macro-sizes, $\tilde{h} = 0.1 \mu m - 1 mm$, the bulk concentration of the electrolyte is about $\tilde{c}_\infty = 1 - 10^3 mol/m^3$. The heat transfer coefficient between the electrolyte and the environment $\tilde{\alpha}$ depends on many factors, and for each particular case it should be determined experimentally. We assume it changes within a window as $\tilde{\alpha} = 1 - 1000 W/(m^2 K)$. The characteristic temperature, based on Joule heating, is $\tilde{T}_{ch} = 0.1 - 1 K$. This temperature is in correspondence with that found experimentally in [22]: a typical temperature difference between the electrolyte and the environment is about several degrees.

From the analysis of the above mentioned dimensional values, it follows that the dimensionless parameters vary within the range: $\nu = 10^{-6} - 10^{-2}$, $\varkappa = 0.05 - 0.5$, $Ra = 10^{-6} - 100$. It is assumed that the other dimensionless parameters can be fixed as $p = 5$ (see [6, 8, 11]) and $Le = 0.013$ (for water). We assume that $Bi = 10^{-2}$ is taken.

The problem has three parameters: ν , Ra , and \varkappa . This fact greatly complicates the numerical investigation of the problem. The first small parameter, the Debye number, makes the problem singular and forms a thin EDL near the boundaries of the investigated domain, $y = 0$ and $y = 1$. An asymptotic expansion with respect to the Debye number ν is investigated in [5, 6, 8], and the application of the results of [5] to our problem will be developed in the next section.

ANALYTICS

A. Quiescent solution

For the one-dimensional steady-state solution, $\partial/\partial t = \partial/\partial x = 0$, the system (1)–(4) can be integrated once with respect to y . Taking into account the BCs (6)–(7) and the definition of the electric current j (8), we get the following system.

$$\rho E + \frac{dK}{dy} = j, \quad KE + \frac{d\rho}{dy} = j, \quad (10)$$

$$\nu^2 \frac{dE}{dy} = -\rho, \quad \frac{d^2 T}{dy^2} + Bi E j = 0, \quad (11)$$

$$y = 0: \quad c^+ = p, \quad \Phi = 0, \quad -\frac{dT}{dy} + Bi T = 0, \quad (12)$$

$$y = 1: \quad c^+ = p, \quad \Phi = \Delta V, \quad \frac{dT}{dy} + Bi T = 0, \quad (13)$$

where $E \equiv d\Phi/dy$ and j in the 1D statement coincides with $-\mathbf{I} \cdot \mathbf{e}_y$. This system describes the 1D solution, which is decoupled from the hydrodynamics, $U = V = 0$, and does not depend on the parameter Ra .

Note that the electrostatic part of the system is also decoupled from the thermal part and can be solved independently from T . Equations (10)–(11) turn into one nonlinear ordinary differential equation (ODE) (see [2] and [23]):

$$\nu^2 \frac{d^2 E}{dy^2} + \left[j(y_m - y) - \frac{\nu^2}{2} E^2 \right] E + j = 0. \quad (14)$$

Here, y_m is an unknown constant of integration which will be determined later. This nonlinear second order ODE has to be solved along with the three remaining boundary conditions: $y = 0$: $c^+ = p$; $y = 1$: $c^+ = p$; $\Phi(1) - \Phi(0) = \Delta V$. For extreme nonequilibrium conditions (see [8] for details), as $\nu \rightarrow 0$ and $E > O(\log \nu) = O(1/\nu)$, $d/dy = O(1)$, the ODE (14) asymptotically turns into a cubic algebraic equation in E ,

$$\left[\frac{\nu^2}{2} E^2 - j(y_m - y) \right] E = 0, \quad (15)$$

and we can skip the first two BCs and keep the third one,

$$\Phi(1) - \Phi(0) = \Delta V. \quad (16)$$

This is valid if $O(|\log \nu|) < \Delta V < O(1/\nu)$ [23]. Equation (15) has three solutions, but only two of them make physical sense ($E > 0$ and $E = 0$). The first one is valid in the space charge region (SCR),

$$E = \frac{1}{\nu} \sqrt{2j(y_m - y)} \text{ for } 0 < y < y_m, \quad (17)$$

$$\nu \Phi = \frac{2\sqrt{2}}{3j} (jy_m)^{3/2} - \frac{(2jy_m - 2jy)^{3/2}}{3j},$$

with the charge density

$$\rho = -\nu^2 \frac{dE}{dy} = \frac{\nu \sqrt{j}}{\sqrt{2(y_m - y)}}, \quad (18)$$

which has an integrable singularity that vanishes in the next approximation. Near the charge selective surface, $y = 0$, an electric double layer (EDL) forms and for the extreme non-equilibrium case, the influence of the EDL is asymptotically small [5].

Thus, from (17) and (16) we can not only get a physical meaning for the integration constant y_m , which is the length of the SCR, but also get its value:

$$y_m = \frac{9^{1/3} \nu^{2/3} \Delta V^{2/3}}{2j^{1/3}}, \quad y_m = O(\nu^{2/3} (\log \nu)^{2/3}) \ll 1. \quad (19)$$

The temperature distribution in the SCR is readily found from (11) and (12):

$$T = j \Delta V Bi \left[\frac{1 + \frac{2}{5} y_m}{2 + Bi} \left(1 - y + \frac{1}{Bi} \right) - \frac{2(y_m - y)^{5/2}}{5y_m^{3/2}} \right], \quad (20)$$

The two-term expansion in the SCR for $Bi \rightarrow 0$ gives

$$T_1 = \frac{j \Delta V}{2} \left(1 + \frac{2}{5} y_m \right), \quad (21)$$

$$T_2 = j \Delta V \left[\frac{1}{4} \left(1 + \frac{2}{5} y_m \right) (2y - 1) + \frac{2(y_m - y)^{5/2}}{5y_m^{3/2}} \right].$$

The second solution is valid in the electroneutral region,

$$E = 0, \quad \rho = 0, \quad \Phi = \frac{(2jy_m)^{3/2}}{3j\nu} \text{ for } y_m < y < 1. \quad (22)$$

From (10), (22), and the boundary condition $K(y = y_m) = 0$, we obtain $K = j(y - y_m)$. Using the conservation law $\int_{y_m}^1 K dy = 2$, we obtain the following expression for j ,

$$j = 4 + O(y_m). \quad (23)$$

The temperature distribution in the electroneutral region $y_m < y < 1$ is found by integrating (11) and using the BCs (13) and satisfying the continuity of the temperature and its derivative at $y = y_m$. It has the form

$$T = Bi \frac{j \Delta V}{2 + Bi} \left(1 + \frac{2}{5} y_m \right) \left(1 - y + \frac{1}{Bi} \right). \quad (24)$$

The two-term expansion in the electroneutral region for $Bi \rightarrow 0$ gives

$$T_1 = \frac{j \Delta V}{2} \left(1 + \frac{2}{5} y_m \right) \approx \frac{j \Delta V}{2}, \quad (25)$$

$$T_2 = \frac{j \Delta V}{4} \left(1 + \frac{2}{5} y_m \right) (2y - 1) \approx \frac{j \Delta V}{4} (2y - 1).$$

B. Slip velocity

Let us impose long-wave perturbations, and so the independent variables of the system in the SCR are not constant with respect to x but instead are slowly varying functions: $\partial/\partial x \ll \partial/\partial y$. Then we get non-zero velocity components $V \ll U$. Equation (3) turns into the following (see [8, 23]),

$$\frac{\partial \Pi}{\partial y} = \frac{\varkappa}{2} \frac{\partial E^2}{\partial y} + Ra T, \quad \frac{\partial^2 U}{\partial y^2} = \frac{\partial \Pi}{\partial x} - \varkappa \frac{\partial \Phi}{\partial x} \frac{\partial E}{\partial y}, \quad (26)$$

with the boundary conditions

$$y = 0: \quad U = 0, \quad y = y_m: \quad \frac{\partial U}{\partial y} = 0, \quad \Pi = 0. \quad (27)$$

Upon excluding pressure from this system, integrating twice, and using the boundary conditions (27), we obtain the electro-osmotic slip velocity, $U_m \equiv U(y = y_m)$,

$$U_m = -\frac{\varkappa}{8} \Delta V^2 \frac{1}{j} \frac{\partial j}{\partial x} + \frac{3}{16} \nu^2 \Delta V^2 Ra \frac{\partial}{\partial x} \left(\frac{T_m}{j} \right), \quad (28)$$

with $T_m \equiv T(y = y_m)$. At $Ra = 0$ this relation coincides with the famous Rubinstein–Zaltzman formula for the slip velocity [5]. The contribution of the term responsible for the thermal effects is significant for very large Rayleigh numbers $Ra = O(1/\nu^2)$, and the influence of the thermo-effects in the SCR is negligible. This hypothesis will be confirmed by the numerics.

In order to solve the heat transfer equation in the electroneutral region, an additional BC for the temperature is required. Such a BC can be easily obtained from the 1D solution (20) and with the assumption $y_m \ll 1$:

$$-\frac{\partial T_m}{\partial y} + Bi T_m = j Bi \Delta V. \quad (29)$$

This BC has “a source term” in the right-hand side, which is the origin of the thermal instability.

C. The electroneutral region and instability of the 1D steady state.

In the electroneutral diffusion region, $y_m < y < 1$, Eqs. (1)–(4) along with the boundary conditions taken from the solution in the SCR turn into

$$\frac{\partial^4 \Psi}{\partial x^4} + 2 \frac{\partial^4 \Psi}{\partial x^2 \partial y^2} + \frac{\partial^4 \Psi}{\partial y^4} = Ra \frac{\partial T}{\partial x}, \quad (30)$$

$$\begin{aligned} y = y_m : \quad \Psi &= 0, & \frac{\partial \Psi}{\partial y} &= U_m, \\ y = 1 : \quad \Psi &= 0, & \frac{\partial \Psi}{\partial y} &= 0. \end{aligned} \quad (31)$$

Upon neglecting the thermal effects ($Ra = 0$), this formula turns into the Rubinstein–Zaltzman relation, (94) in [5]. The second term of the right-hand side of (36), which is proportional to Ra , is responsible for the thermal effects. This relation, along with the Rubinstein–Zaltzman formula, is not applicable for long perturbations $k \rightarrow 0$, because, for the sake of simplicity, the influence of the Debye layer in the upper membrane has not been taken into account.

The main conclusion from the formula described by Eq. (36) (Fig. 2) is that the system is stabilized by the thermal effects at $Ra > 0$ and is destabilized when $Ra < 0$. Changing of the sign of Ra is nothing more than the rotation of the system at 180° relative to the direction of gravity. The relation (36) will be analyzed in the next section, along with our numerical results. In the problem, there are two competing mechanisms of instability, which can

$$\frac{\partial K}{\partial t} + U \frac{\partial K}{\partial x} + V \frac{\partial K}{\partial y} = \frac{\partial^2 K}{\partial x^2} + \frac{\partial^2 K}{\partial y^2}, \quad (32)$$

$$\begin{aligned} y = y_m : \quad K &= 0, \\ y = 1 : \quad \int_{y_m}^1 K dy &= 2, \end{aligned} \quad (33)$$

$$\frac{\partial^2 T}{\partial x^2} + \frac{\partial^2 T}{\partial y^2} = 0, \quad (34)$$

$$\begin{aligned} y = y_m : \quad -\frac{\partial T}{\partial y} + Bi T &= j Bi \Delta V, \\ y = 1 : \quad \frac{\partial T}{\partial y} + Bi T &= 0. \end{aligned} \quad (35)$$

In order to study the linear stability of the solution, we superimpose on it small sinusoidal perturbations of the form $f = f_0(y) + \hat{f}(y) \exp(ikx + \lambda t)$, $\hat{f} \rightarrow 0$, where k is the wavenumber and λ is the growth rate.

Linearizing with respect to the perturbations turns the nonlinear system (30)–(35) into a system of linear ODEs, which can be solved analytically. Leaving only the leading order term in the expansion with respect to small Bi , we get the condition for marginal stability, $\lambda = 0$:

$$1 = \frac{\varkappa}{8} \Delta V^2 \frac{k^3 \cosh k - \sinh^3 k}{4 \sinh k (k^2 - \sinh^2 k)} - Ra \frac{\Delta V}{8} Bi \frac{k^2 (\sinh k - k \cosh k)^2 - (k^2 - \sinh^2 k)^2}{k^4 \sinh^2 k (k^2 - \sinh^2 k)}. \quad (36)$$

be clearly elucidated by the analytical solution Eq. (36). The first one is the Zaltzman–Rubinstein electrokinetic instability, characterized by the first term in the right-hand side of Eq. (36). The second is connected with the Joule heating, and is characterized by the second term in the right-hand side of Eq. (36). For the case when the heating is absent ($Ra = 0$) the instability is caused by the Coulomb force in the SCR, $0 < y < y_m$, and the corresponding formation of a slip velocity (28) at $y = y_m$. The nonuniformity of the slip velocity leads to the electrokinetic instability [8]. The competing mechanism is associated with the Joule heating, mainly in the electroneutral region, $y_m < y < 1$. The second mechanism is connected with heating and the thermic expanding of the liquid, but it is totally different from the Rayleigh–Bénard convection and the instability is caused by an induced nonuniformity of the conductivity in the elec-

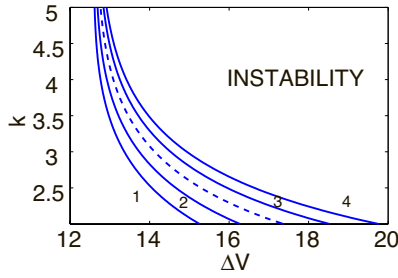


FIG. 2. Marginal stability curves described by Eq. (36), the wave number k vs. the voltage ΔV , for $\varkappa = 0.2$: 1: $Ra = -1000$, 2: -500 , 3: 500 , 4: 1000 ; dot-dashed line: $Ra = 0$

trolyte.

It is worthwhile considering here the physical aspects of the electrokinetic and thermal instabilities, and comparing them. For the sake of simplicity, we assume that in the electroneutral region, $y_m < y < 1$, the length of the SCR is negligibly small, $y_m = 0$, and the final electroneutral domain would be $0 < y < 1$.

In the case of a pure electrokinetic instability, $Ra = 0$, $\varkappa \neq 0$, the perturbation of the conductivity \hat{K} is at the same time the perturbation of the ion flux $\hat{j} = \partial \hat{K} / \partial y|_{y=0}$, and in a small vicinity of $y = 0$ we have as follows,

$$K = jy + \hat{K}(y) \exp(ikx) + CC, \quad \hat{K} = \hat{j}y + O(y^2).$$

The perturbation of the ion flux near $y = 0$ produces an electro-osmotic slip velocity components. It is readily found from Eq. (28) and the mass conservation equation,

$$\hat{U} = -\frac{i}{32} \varkappa k \Delta V^2 \hat{j} + O(y), \quad \hat{V} = -\frac{\varkappa}{32} k^2 \Delta V^2 \hat{j} y + O(y^2), \quad (37)$$

and \hat{V} is in anti-phase with the ion flux \hat{j} .

The electric conductivity \hat{K} is changing in time according to Eq. (32). The terms in the right-hand side of this equation correspond to the dissipation and cannot be the origin of instability; for our qualitative speculations these terms are omitted and the truncated Eq. (32) has form,

$$\frac{\partial \hat{K}}{\partial t} \approx -4\hat{V}, \quad \text{or taking into account } \hat{K} = \hat{j}y + O(y^2), \quad (38)$$

$$\frac{\partial \hat{j}}{\partial t} \approx \frac{\varkappa}{8} k^2 \Delta V^2 \hat{j} + O(y).$$

To be more clear we have changed $\lambda \hat{K}$ to $\partial \hat{K} / \partial t$. Hence, the initial perturbation of \hat{j} has a positive feedback and develops instability, see Fig. 4(a). Velocity components \hat{U} and \hat{V} are the origin of the liquid circulation.

For the pure thermal case, $\varkappa = 0$, $Ra \neq 0$, see Fig. 4 (b) and (c), the slip velocity is absent, $\hat{U}_m = 0$, but at $y = 0$ there is a “source” of energy proportional to the ion flux \hat{j} : the liquid is either heated and or cooled at

$y = 0$ in phase with \hat{j} , see Eq. (30). In other words, the temperature increases in the regions with a larger ion flux (or larger electric conductivity) and decreasing in the places with a smaller one.

The liquid is squeezed out of the places with high temperature and is drawn to places with lower temperature; the vertical component of velocity \hat{V} is proportional to $\Delta V Ra \hat{j}$, see Eq. (35). For $Ra > 0$ \hat{V} is in phase with \hat{j} and for $Ra < 0$ \hat{V} is in anti-phase with \hat{j} , see Appendix.

Taking for the electric conductivity \hat{K} the truncated Eq. (32) with omitted dissipation terms,

$$\frac{\partial \hat{K}}{\partial t} \approx -4Ra \Delta V Bi V_T(y) \hat{j}, \quad (39)$$

it is easy to see that for $Ra > 0$ $\partial \hat{K} / \partial t$ is in anti-phase with the right-hand-side of (39) and, hence, the perturbations decay. For $Ra < 0$ $\partial \hat{K} / \partial t$ is in phase with the right-hand-side of (39). Hence, the initial perturbations of \hat{j} have a positive feedback and develop instability. One can see that the physical mechanism of the thermal instability is very different from the Rayleigh–Bénard convection.

I. NUMERICAL SOLUTION

This investigation is complemented by numerical calculations of the linear stability of the 1D quiescent solution with respect to sinusoidal perturbations with wave number k , $f = f_0 + \hat{f} \exp(\lambda t + ikx)$ for $f = \{c^\pm, \Phi, V, T\}$. The Galerkin pseudo-spectral τ -method with Chebyshev polynomials taken as the basic functions [24] is employed to discretize the eigenvalue problem. The generalized matrix eigenvalue problem is solved by the QR algorithm [24]. The number of Chebyshev functions in the expansion is up to 512.

The two competing mechanisms of instability are determined by the parameters \varkappa and Ra . The relation between these parameters determines which of the instability mechanisms will be decisive for the destabilization of the system. Fig. 4 presents the numerically obtained marginal stability curves for different values of \varkappa and Ra . For the case without thermo-effects, $Ra = 0$, the numerics are compared with the analytics of Zaltzman and Rubinstein [8]: our numerical approach is in good correspondence with the asymptotical results. The case $Ra = 0$ separates the destabilizing and stabilizing effects of the Joule heating. The boundary value $|Ra| = 50$ is taken in the figures: for larger $|Ra|$, the results coincide with graphical accuracy with those obtained at the boundary value $|Ra| = 50$. It can be seen that the analytics (Fig. 2) can not claim very much accuracy, but it can qualitatively explain the physical aspects of the problem.

For $Ra < 0$, with decreasing \varkappa or increasing $|Ra|$, the heat effects prevail over the electrokinetic effects and a drastic change of instability modes occurs: the critical

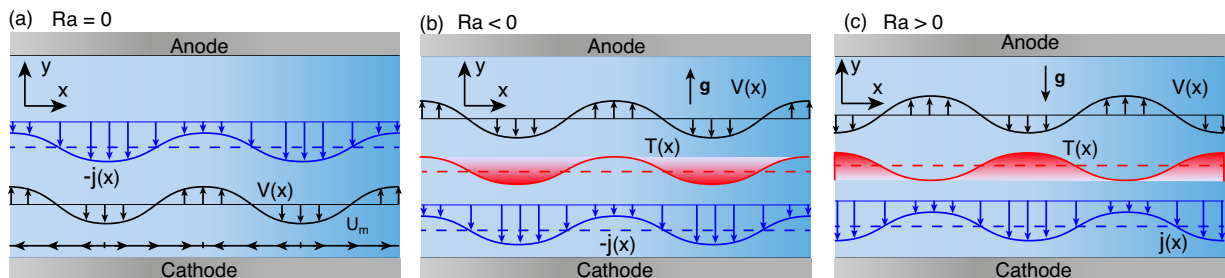


FIG. 3. Interpretation of the physical mechanism of the electrokinetic, (a), and thermal, (b) and (c), instabilities. Only a small region near $y = 0$ is considered.

voltage ΔV_* decreases dramatically. Moreover, the short-wave instability changes to a long-wave instability. Universal character of the behavior of the long-wave marginal stability curves near ΔV_* can be seen from Figs. 4(a)–4(b).

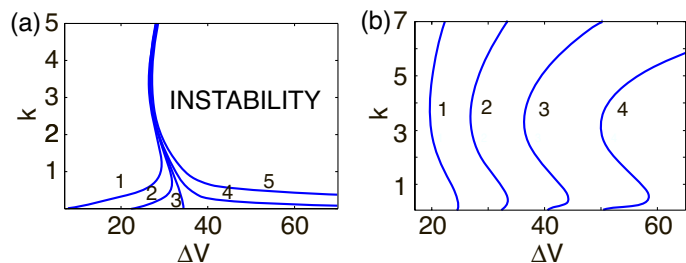


FIG. 4. Marginal stability curves of the numerical solution, the wave number k vs. the voltage ΔV for $\nu = 0.01$, (a) $\varepsilon = 0.2$, Ra : 1: -50, 2: -10, 3: 0, 4: 10, 5: 50 and (b) $Ra = -10$, ε : 1: 0.5, 2: 0.2, 3: 0.1, 4: 0.05.

CONCLUSION

A new kind of instability caused by Joule heating near charge selective surfaces and its influence on the electrokinetic instability are investigated theoretically. A simple asymptotic relation for the marginal stability is derived; it shows that the Joule heating can drastically destabilize the one-dimensional equilibrium. The study

is complemented by a numerical investigation of the instability, which is in qualitative agreement with the analytical solution. The physical mechanism of the thermal instability is found to be very different from that of Rayleigh–Bénard convection, and the instability is caused by an induced nonuniformity of the electrical conductivity in the electrolyte. In addition, the previous discrepancies between the experiments [7] and the theory [12] have shown, in the present study, a trend of better agreement by taking into account the Joule heating for the appropriate Rayleigh numbers.

ACKNOWLEDGMENTS

EAD, GSG and NYK were supported, in part, by the Russian Foundation for Basic Research (Project Nos. 15-08-02483-a, 13-08-96536-r.yug.a, 14-08-31260 mol-a, and 14-08-00789-a). EAD and SA are grateful for the financial support from France in the framework of the “Investments for the future” Programme IdEx Bordeaux, reference ANR-10-IDEX-03-02. The authors greatly appreciate the enthusiastic help of Maksim Chernyshenko, the Mathematical High School # 4 student of the city of Krasnodar, in our numerical calculations.

REFERENCES

[1] I. Rubinstein and L. Shtilman, Voltage against current curves of cation exchange membranes, *J. Chem. Soc.*

Faraday Trans. II, Vol. 75,1979, pp. 231-246.

- [2] V. A. Babeshko, V. I. Zabolotsky, E. V. Kirillova, and M. A.-K. Urtenov, Dekompozicija sistem uravnenij Nernsta-Planka-Puassona [in Russian], *Dokl. Akad. Nauk*, Vol. 344, No 4, 1995, pp. 485-446.
- [3] V. V. Nikonenko, V. I. Zabolotsky, and N. P. Gnusin, Electric transport of ions through diffusion layers with impaired electroneutrality, *Sov. Elektrochem.*, Vol. 25, 1989, pp. 301-310.
- [4] K. T. Chu and M. Z. Bazant, Siam J., Electrochemical thin films at and above the classical limiting current, *Appl. Math.*, Vol. 65, 2005, pp. 1485-1505.
- [5] I. Rubinstein and B. Zaltzman, Electro-osmotically induced convection at a permselective membrane, *Phys. Rev. E*, Vol. 62, No 2, 2000, pp. 2238-2251.
- [6] I. Rubinstein and B. Zaltzman, Wave number selection in a nonequilibrium electro-osmotic instability, *Phys. Rev. E*, Vol. 68, 2013, Paper number 032501.
- [7] S. M. Rubinstein, G. Manukyan, A. Staicu, I. Rubinstein, B. Zaltzman, R. G. H. Lammertink, F. Mugele, and M. Wessling, Direct Observation of a Nonequilibrium Electro-Osmotic Instability, *Phys. Rev. Lett.* Vol. 101, 2008, Paper number 236101.
- [8] B. Zaltzman and I. Rubinstein, Electro-osmotic slip and electroconvective instability *J. Fluid Mech.*, Vol. 579, 2007, pp. 173-226.
- [9] H.-C. Chang, G. Yossifon, and E. A. Demekhin, Nanoscale Electrokinetics and Microvortices: How Microhydrodynamics Affects Nanofluidic Ion Flux, *Annu. Rev. Fluid Mech.* Vol. 44, 2012, pp. 401-426.
- [10] V. S. Pham, Z. Li, K. M. Lim, J. K. White, and J. Han, *Phys. Rev. E* **86**, 046310 (2012).
- [11] H.-C. Chang, E. A. Demekhin, and V. S. Shelistov, Competition between Dukhins and Rubinsteins electrokinetic modes, *Phys. Rev. E*, Vol. 86, 2012, Paper number 046319.
- [12] E. A. Demekhin, N. V. Nikitin, and V. S. Shelistov, Direct Numerical Simulation of Electrokinetic Instability and Transition to Chaotic Motion, *Phys. Fluids*, Vol. 25, 2013, p. 122001.
- [13] V. S. Shelistov, N. V. Nikitin, V. A. Kiriya, and E. A. Demekhin, A Sequence of Electrokinetic Instability Bifurcations Resulting in a Chaotic Flow Regime *Doklady Physics*, Vol. 59, No 4, 2014, pp. 166-169.
- [14] V. S. Shelistov, E. A. Demekhin, and G. S. Ganchenko, Electrokinetic instability near charge-selective hydrophobic surfaces, *Phys. Rev. E*, Vol. 90, 2014, Paper number 013001.
- [15] E. A. Demekhin, N. V. Nikitin, and V. S. Shelistov, Three-dimensional coherent structures of electrokinetic instability, *Phys. Rev. E*, Vol. 90, 2014, Paper number 013031.
- [16] W.M. Saslow, Joule heating rate need not equal $(IR)-R^{-2}$, where R is the Ohmic resistance: The case of voltaic cells, *Phys. Rev. E*, Vol. 59, 1999, pp. 1343(R)-1346(R).
- [17] D. Erickson, D. Sinton, and D. Li, Joule heating and heat transfer in poly (dimethylsiloxane) microfluidic systems, *Lab on a Chip*, Vol. 3, 2003, pp. 141-149.
- [18] G. Hu, Q. Xiang, R. Fu, B. Xu, R. Venditti, and D. Li, Electrokinetically controlled real-time PCR in microchannel using Joule heating effect, *Analytica Chimica Acta*, Vol. 557, 2006, 146-151.
- [19] A. Sharma and S. Chakraborty, Semi-analytical solution of the extended Graetz problem for combined electroosmotically and pressure-driven microchannel flows with step-change in wall temperature, *International Journal of Heat and Mass Transfer* Vol. 51, 2008, 4875-4885.
- [20] M. M. Rahman, R. Saidur, and N. A. Rahim, Conjugated effect of joule heating and magneto-hydrodynamic on double-diffusive mixed convection in a horizontal channel with an open cavity, *International Journal of Heat and Mass Transfer* Vol. 54, 2011, pp. 3201-3213.
- [21] H. Yavari, A. Sadeghi, M. H. Saidi, and S. Chakraborty, Combined influences of viscous dissipation, non-uniform Joule heating and variable thermophysical properties on convective heat transfer in microtubes, *International Journal of Heat and Mass Transfer*, Vol. 55, 2012, pp. 762-772.
- [22] V. I. Zabolocky and V. V. Nikonenko, *Perenos ionov v membranah*, Nauka, Moscow (1996) [in Russian].
- [23] I. Rubinstein and B. Zaltzman, Electro-osmotic slip of the second kind and instability in concentration polarization at electro dialysis membranes, *Math. Mod. Meth. Appl. Sci.*, Vol. 11, 2011, 263-300.
- [24] S. A. Orszag, Accurate solution of the Orr-Sommerfeld stability equation, *J. Fluid Mech.*, Vol. 50, 1971, pp. 689-703.